Thermodynamically consistent phase-field theory including nearest-neighbor pair correlations

Kristian Blom [1], Noah Ziethen [2], David Zwicker [2] and Aljaž Godec [1,*]

[1] *Mathematical bioPhysics group, Max Planck Institute for Multidisciplinary Sciences, Göttingen 37077, Germany*

[2] *Theory of Biological Fluids, Max Planck Institute for Dynamics and Self-Organization, Göttingen 37077, Germany*

(Received 6 April 2022; revised 11 July 2022; accepted 17 January 2023; published 22 February 2023)

Most of our current understanding of phase separation is based on ideas that disregard correlations. Here we illuminate unexpected effects of correlations on the structure and thermodynamics of interfaces and in turn phase separation, which are decisive in systems with strong interactions. Evaluating the continuum limit of the Ising model on the Bethe-Guggenheim level, we derive a Cahn-Hilliard free energy that takes into account pair correlations. For a one-dimensional interface in a strip geometry, these are shown to give rise to an *effective interface broadening* at interaction strengths near and above the thermal energy, which is verified in the Ising model. Interface broadening is the result of an entropy-driven interface delocalization, which is not accounted for in the widely adopted mean field theory. Pair correlations are required for thermodynamic consistency as they enforce a thermodynamically optimal local configuration of defects and profoundly affect nucleation and spinodal decomposition at strong coupling.

DOI: 10.1103/PhysRevResearch.5.013135

I. INTRODUCTION

Instigated by the seminal works of Cahn and Hilliard [1–3], phase separation, the process through which homogeneous mixtures demix into distinct phases, has attracted considerable attention in a variety of fields, including physics [4–13], mathematics [14–16], chemistry [17–20], material science [21–23], and recently biology [24–27]. Our understanding of phase separation in systems in [28,29] and out [30,31] of equilibrium is mostly based on mean field (MF) ideas [32], also known as regular solution [1], Bragg-Williams [33], or Flory-Huggins [34,35] theory (for recent works see [10–13,25–27,36–41]). MF theory neglects correlations whose importance grows with the strength of interactions [4]. For example, capillary wave fluctuations [41,42] are *not* captured in MF theories. This questions whether MF ideas correctly describe the physics of strongly interacting systems [39,43].

Various refined techniques have been developed beyond the MF approximation, including the cavity method [44], random phase approximation [45,46], self-consistent field theory [47], and field-theoretic approaches close to criticality [48]. Yet, these techniques either do not apply to nonuniform systems, or are applicable in a limited range of interaction strengths. As a result, the phenomenology of phase separation in the strong-coupling limit remains largely unexplored, and thus poorly understood.

Here we employ the Bethe-Guggenheim (BG) approximation [49–52] that includes nearest-neighbor pair correlations. By evaluating the thermodynamic limit of a spatially inhomogeneous nearest-neighbor interacting Ising model, we derive a Cahn-Hilliard free energy on the BG level that effectively accounts for the effects of capillary wave fluctuations. We investigate the phenomenology of interfaces and phase condensation, and find at sufficiently strong interactions an *effective interface broadening* not accounted for by MF theories. We corroborate the broadening with simulations, and exact results in the infinite-interaction limit. Furthermore, via numerical simulations of the Cahn-Hilliard equation [53], we analyze nucleation kinetics, and observe amplified nucleation barriers and a nonmonotonic dependence of the interface steepness and critical nucleus size on the interaction strength.

II. MOTIVATING EXAMPLE: INTERFACE DELOCALIZATION

An intriguing phenomenon in strongly interacting systems is interface delocalization [54–65]. Consider a two-dimensional Ising model with ferromagnetic interaction J (in units of k_BT) in a strip geometry (i.e., height $\gg$ length) in the two-phase regime. Imposing periodic boundary conditions in the vertical direction, and thermodynamically coexisting phase compositions at the left and right edges, the *instantaneous* concentration of down spins projected onto the x direction, $\varphi_i(x)$, develops an interface [see Fig. 1(a)], whose position x_i is defined implicitly via $\varphi_i(x_i) = 1/2$. In the absence of boundary effects, shifting an instantaneous interface $\varphi_i(x_i) \to \varphi_i(x_i + dx_i)$ costs no energy. However, x_i near the boundaries are entropically penalized, as they allow only for a limited bandwidth of capillary wave fluctuations [see Fig. 1(a), top] [64–67]. As a result, we find at weak to moderate J that the probability density of instantaneous interface

*agodec@mpinat.mpg.de

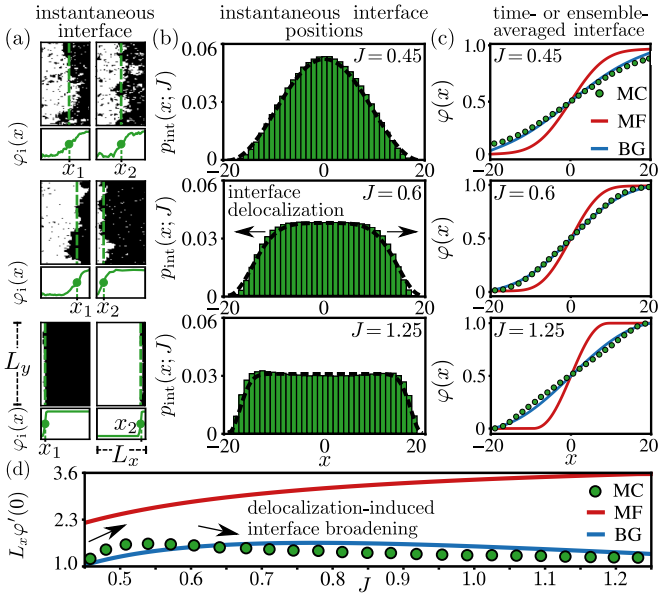

FIG. 1. (a) Realizations of spin configurations (top) and corresponding *instantaneous* interfaces (bottom) in a two-dimensional Ising strip with lattice constant δ and dimensions $(L_x, L_y) = (40, 120)\delta$, for different $J = \{0.45, 0.6, 1.25\}$ obtained from Monte Carlo simulations (see Appendix A for details). The circle and dashed line denote the position of the instantaneous interface. (b) Statistics of interface positions derived from simulations (green) and given by Eq. (4) (black dashed line) via a mapping onto the Brownian excursion problem. (c) Corresponding *ensemble-averaged* concentration profile along the x axis alongside theoretical predictions of mean field (MF; red) and Bethe-Guggenheim (BG; blue) theory. (d) Scaled interface steepness $L_x\varphi'(0) \equiv L_x\partial_x\varphi(x)|_{x=0}$ as a function of J.

positions, defined as $p_{\rm int}(x;J)$, is peaked at the center [see Fig. 1(b), top]. At larger J the amplitude of capillary waves diminishes [see Fig. 1(a), center and bottom], and a transition occurs that delocalizes the instantaneous interface [see Fig. 1(b), center and bottom as well as [60–65]]. A sharp but delocalized instantaneous interface becomes effectively broader upon *time or ensemble averaging* over respective interface positions [see Figs. 1(c) and 1(d)]. Exact results in the regime $J \to \infty$ have confirmed the interface broadening [60–63], whereas it is known that MF theory fails to account for it [64,68]. A comprehensive theory that captures the broadening transition due to the instantaneous interface delocalization remains elusive. This example therefore motivates a deeper and more systematic analysis of interfaces and phase separation in the strong interaction limit.

III. OUTLINE

First, we present in Sec. IV a derivation of the probability density of instantaneous interface positions based on a mapping onto the Brownian bridge problem [Eq. (4)]. Thereafter, we present in Sec. V a detailed microscopic derivation of the Cahn-Hilliard–type phase-field free energy starting from an anisotropic two-dimensional Ising model using the BG approximation [Eqs. (27)–(29)]. In Sec. VI we analyze the field theories by determining the one-dimensional equilibrium concentration profile, interface steepness, interface stiffness, and the critical wavelength of stable perturbations. Furthermore, we analyze nucleation kinetics via numerical simulations of the newly derived Cahn-Hilliard equation. Finally, in Sec. VII we conclude and reflect on possible future directions. Details of simulations and calculations are shown in a series of Appendixes A–G.

The Appendixes are organized in the order they appear in the main paper. First, we present in Appendix A a detailed description of the Monte Carlo simulations that are shown in Fig. 1. Appendixes B and C are devoted to the derivation of the Cahn-Hilliard free energy starting from a two-dimensional Ising model using the mean field (Appendix B) and Bethe-Guggenheim (Appendix C) approximations, respectively. The latter is also discussed in Sec. V, but here we provide some more technical details. Next, in Appendixes D and E we analyze the field theories by determining the one-dimensional equilibrium concentration profile, interface steepness, interface width, and critical wavelength of stable perturbations. In Appendix F we probe the accuracy of both approximations by comparing them with exact results for system sizes which are amendable to exact solutions. Finally, in Appendix G we present details on the numerical simulations of nucleation shown in Fig. 5.

IV. STATISTICS OF INSTANTANEOUS INTERFACE POSITION

Here we derive the probability density of instantaneous interface positions, based on the analogy with Brownian bridges, used for Fig. 1(b) (black dashed lines). Furthermore, in Sec. IV C we prove the convergence to a uniform distribution in the limit $J \to \infty$, which we use in Sec. VI B to disentangle interface delocalization from the instantaneous interface width.

A. Main idea

Neglecting overhangs, one can map the statistics of instantaneous interfaces onto a one-dimensional confined Brownian bridge problem (see Fig. 2) [65]. The idea is to treat the respective bulk phases as "pure" (i.e., homogeneous) and the interface (i.e., domain wall) as a random walk located between two hard walls at $x = 0$ and L_x. Then, in the continuum limit the interface is equivalent to a Brownian trajectory where the vertical coordinate y plays the role of time and the diffusion coefficient is proportional to $1/4\Lambda$ (see Sec. IV B), where

$$\Lambda = \sinh(2J + \ln\tanh J) \tag{1}$$

is the exact interface stiffness for the two-dimensional Ising model [69,70]. Periodic boundary conditions in the y direction render the trajectories Brownian bridges.

B. Derivation of interface statistics

We parametrize the domain wall as a Brownian motion $\{x_y^{\rm i}\}_{0\leqslant y\leqslant L_y}$ where y plays the role of time (or contour length in the polymer context). Then, the Green's function of the interface with diffusion coefficient D follows the Edwards

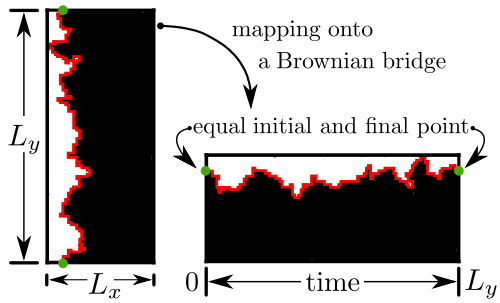

FIG. 2. Mapping the instantaneous interface (red line, left) onto a Brownian bridge (red line, right). Neglecting overhangs, and treating the bulk phases (black and white regions) as homogeneous, the instantaneous interface becomes a Brownian trajectory where the vertical coordinate y plays the role of time. Greens dots indicate the equal positions of the interface at 0 and L_y, rendering the interface a Brownian bridge.

equation with absorbing boundary conditions at the walls

$$\begin{aligned} \partial_y G(x,y|x_0) &= D\nabla_x^2 G(x,y|x_0), \\ G(x,0|x_0) &= \delta(x-x_0), \\ G(0,y|x_0) &= G(L_x,y|x_0) = 0, \quad \forall\, y\in[0,L_y]. \end{aligned} \tag{2}$$

The general solution to Eq. (2) is

$$G(x,y|x_0)=\frac{2}{L_x}\sum_{k=1}^{\infty}\sin\left(\frac{k\pi x}{L_x}\right)\sin\left(\frac{k\pi x_0}{L_x}\right)\exp\left(\frac{-\pi^2k^2Dy}{L_x^2}\right).$$

Particularly interesting is the mean-squared displacement, which for $y \ll D/L_x^2$ is given by $\langle(x-x_0)^2\rangle\simeq 2Dy$, where $\simeq$ stands for asymptotic equality, i.e., $A\simeq B$ when $A/B\to 1$. Such a scaling is expected for a freely diffusing particle. Now we recall the exact results of Abraham [69] and Fisher [70] who found that for the two-dimensional Ising strip the interface width should scale as $\langle(x-x_0)^2\rangle \propto y/\Lambda$ where the proportionality factor includes some lattice length scale and Λ is the surface stiffness given by Eq. (1). This outcome allows us to relate the diffusion coefficient D to the surface stiffness

$$D\propto\frac{1}{2\Lambda}. \tag{3}$$

Under periodic boundary conditions in the y direction the interfaces have an equal position at $y=0$ and L_y, also known as Brownian bridges. In this case the propagator is simply given by $G(x,L_y|x)$. We can now calculate the probability density to have an interface located at position x, which upon normalization is given by

$$\begin{aligned} p_{\rm int}(x;J) &= \frac{G(x,L_y|x)}{\int_0^{L_x}G(x,L_y|x)dx} \\ &= \frac{1}{L_x}\frac{\vartheta_3(0,\mathrm{e}^{-\alpha_J})-\vartheta_3(\pi x/L_x,\mathrm{e}^{-\alpha_J})}{\vartheta_3(0,\mathrm{e}^{-\alpha_J})-1}, \end{aligned} \tag{4}$$

where $\alpha_J\equiv\pi^2DL_y/L_x^2$ and $\vartheta_3(a,x)$ is Jacobi's elliptic theta of the third kind. The second equality can be obtained from the definition of $\vartheta_3(a,x)$. Plugging Eq. (3) for the diffusion coefficient (with proportionality factor equal to unity) into Eq. (4), we obtain the black dashed lines in Fig. 1(b). As long as $J\ll 1$ we have $\Lambda\ll 1$ and thus $\alpha_J\gg 1$. Accordingly, Eq. (4) predicts instantaneous interfaces to be localized with a probability density $p_{\rm int}(x;J)\propto\sin(\pi x/L_x)^2$ [see Fig. 1(b), top panel]. Conversely, for sufficiently large J we find $\Lambda\gg 1$ and hence $\alpha_J\ll 1$, and the interface positions become delocalized [see Fig. 1(b), center and bottom panels].

C. Convergence to the uniform distribution

Next, we show that Eq. (4) converges to a uniform distribution for $J\to\infty$. First, we define $q\equiv\mathrm{e}^{-\alpha_J}$ and rewrite

$$\vartheta_3(\pi x/L_x,\mathrm{e}^{-\alpha_J})=\sum_{n=-\infty}^{\infty}q^{n^2}\mathrm{e}^{\mathrm{i}2\pi xn/L_x}. \tag{5}$$

Since $\alpha_J\geqslant 0$ and $\lim_{J\to\infty}\alpha_J=0$ (uniformly), we find that $\lim_{J\to\infty}\mathrm{e}^{-\alpha_J}$ is equivalent to $\lim_{q\uparrow 1}q$ in Eq. (5). We now use the asymptotic result for $q\uparrow 1$ [71]:

$$\lim_{q\uparrow 1}\sum_{n=-\infty}^{\infty}q^{n^2}\mathrm{e}^{\mathrm{i}2\pi xn/L_x}\simeq\sqrt{\frac{\pi}{-\ln q}}\exp\left(\frac{\pi^2x^2}{L_x^2\ln q}\right). \tag{6}$$

Let us now rewrite Eq. (4) as

$$\begin{aligned} L_xp_{\rm int}(x;J) &= \frac{\vartheta_3(0,\mathrm{e}^{-\alpha_J})-1-\vartheta_3(\pi x/L_x,\mathrm{e}^{-\alpha_J})+1}{\vartheta_3(0,\mathrm{e}^{-\alpha_J})-1} \\ &= 1-\frac{\vartheta_3(\pi x/L_x,\mathrm{e}^{-\alpha_J})-1}{\vartheta_3(0,\mathrm{e}^{-\alpha_J})-1}. \end{aligned} \tag{7}$$

We can now evaluate the limit of Eq. (7) using Eq. (6). Note that Eq. (6) $\gg 1$ for $0<x<L_x$. Hence, we find

$$\begin{aligned} \lim_{J\to\infty}L_xp_{\rm int}(x;J) &\simeq 1-\lim_{q\uparrow 1}\exp\left(\frac{\pi^2x^2}{L_x^2\ln q}\right) \\ &= 1-\lim_{\alpha_J\downarrow 0}\exp\left(-\frac{\pi^2x^2}{L_x^2\alpha_J}\right)\to 1, \end{aligned} \tag{8}$$

for $0<x<L_x$, while we have $p_{\rm int}(0;J)=p_{\rm int}(L_x;J)=0,\ \forall\, J$. This completes the proof. In the forthcoming sections we take the boundaries at $x=\pm L_x/2$, which shifts the coordinates to $x\to x-L_x/2$.

Notably, when $J\to\infty$ a Casimir effect appears in addition (see, e.g., [72,73]) that is *not* captured in Eq. (4), i.e., the entropy due to *bulk* fluctuations is enhanced near the boundaries resulting in "peaks" [see Fig. 1(b), bottom].

V. CAHN-HILLIARD FREE ENERGY INCLUDING PAIR CORRELATIONS

A. Lattice setup and the thermodynamic limit

Spins. For simplicity, and without much loss of generality, we limit the discussion to two-dimensional systems with horizontal and vertical direction $\mathbf{x}=(x,y)\in\mathbb{R}^2$, respectively. We consider $N_\sigma=N_\sigma^x\times N_\sigma^y$ spins $\sigma_{ij}=\pm 1$ with $(i,j)\in(\{1,\ldots,N_\sigma^x\},\{1,\ldots,N_\sigma^y\})$ arranged on a lattice with sides (L_x,L_y). In Fig. 3(a) we provide an example of a square lattice with 16 spins. The lattice spacings between spins are $(\delta_x,\delta_y)=(L_x/N_\sigma^x,L_y/N_\sigma^y)$. The lattice coordination number is denoted with $z=z_x+z_y$, and $\mathbf{z}=\mathrm{diag}(z_x,z_y)$ is a diagonal matrix containing the lattice coordination numbers in each direction. The square lattice in Fig. 3 has $(z_x,z_y)=(2,2)$ and $z=4$.

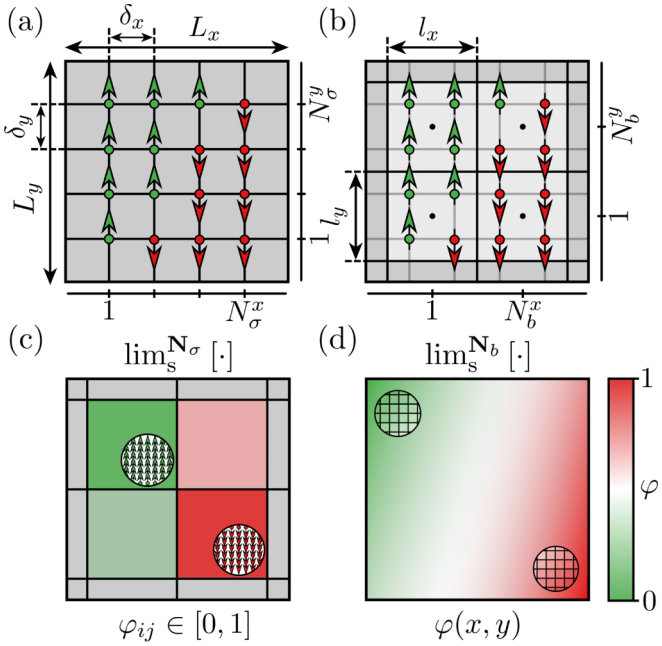

FIG. 3. (a), (b) Lattice setup of the spins (a) and spin blocks (b). $(L_{x,y}, l_{x,y}, \delta_{x,y})$ are the lattice length, spin-block length, and lattice spacing, respectively. The number of spins and spin blocks are denoted with $(N_\sigma^{x,y}, N_b^{x,y})$. Here we consider an example with 16 spins and 4 spin blocks. (c), (d) Thermodynamic limit of the spins (c) and spin blocks (d) defined in Eq. (9). The circles display a graphical magnification of individual spins (c) and spin blocks (d).

Spin blocks. Similar to Kadanoff's block-spin method [74] we place spins into $N_b = N_b^x \times N_b^y$ blocks as shown in Fig. 3(b). Let $\mathbf{b}_{ij}$ with $(i, j) \in (\{1, \ldots, N_b^x\}, \{1, \ldots, N_b^y\})$ denote such a block containing $N_\sigma^b = N_\sigma/N_b$ spins. Consequently, the horizontal and vertical length of each block is given by $(l_x, l_y) = (L_x/N_b^x, L_y/N_b^y)$. The blocks have the same lattice coordination number as the spins. In Fig. 3(b) each block has four spins and aligns with two blocks in the horizontal and vertical direction, respectively.

Thermodynamic limit. To construct a Cahn-Hilliard free energy we introduce the following two scaling limits where we take the number of spins and blocks to infinity while simultaneously keeping the block and lattice length fixed, i.e.,

$$\lim_{\mathrm{s}}^{\mathbf{N}_\sigma}[\cdot] \equiv \lim_{l_x, l_y = \mathrm{const}}^{N_\sigma^x, N_\sigma^y \to \infty}[\cdot],$$
$$\lim_{\mathrm{s}}^{\mathbf{N}_b}[\cdot] \equiv \lim_{L_x, L_y = \mathrm{const}}^{N_b^x, N_b^y \to \infty}[\cdot], \tag{9}$$

where $\mathbf{N}_\sigma$ and $\mathbf{N}_b$ denote the thermodynamic limit of the spins and blocks, respectively. In Figs. 3(c) and 3(d) we give a schematic representation of both limits.

B. Coarse-grained lattice observables

Fraction of down spins. The fraction of down spins in block $\mathbf{b}_{ij}$ (containing N_σ^b spins) is defined as

$$\varphi_{ij}(\{\mathbf{b}_{ij}\}) \equiv \left(N_\sigma^b\right)^{-1} \sum_{mn \in \mathbf{b}_{ij}} (1 - \sigma_{mn})/2, \tag{10}$$

where $mn \in \mathbf{b}_{ij}$ denotes a sum over all indices within block $\mathbf{b}_{ij}$. For a finite number of spins within each block φ_{ij} is a rational number. Applying the first scaling limit in Eq. (9) takes the number of spins within each block to infinity, rendering $\lim_{\mathrm{s}}^{\mathbf{N}_\sigma}[\varphi_{ij}] \in [0, 1]$ a continuous variable [see Fig. 3(c)]. The second limit takes the number of blocks to infinity while simultaneously decreasing their distance, resulting in a continuous differentiable field

$$\lim_{\mathrm{s}}^{\mathbf{N}_b}\left[\lim_{\mathrm{s}}^{\mathbf{N}_\sigma}[\varphi_{ij}]\right] = \varphi(\mathbf{x}),$$

as depicted in Fig. 3(d).

Intrablock defects. Additionally to Eq. (10), we need to define the fraction of intrablock defects inside $\mathbf{b}_{ij}$ in the horizontal and vertical directions, which are given by

$$\zeta_{ij}^{x,y}(\{\mathbf{b}_{ij}\}) \equiv \left(z_{x,y} N_\sigma^b\right)^{-1} \sum_{\langle mn,kl\rangle_{x,y} \in \mathbf{b}_{ij}} |\sigma_{mn} - \sigma_{kl}|, \tag{11}$$

where $\langle mn, kl\rangle_{x,y} \in \mathbf{b}_{ij}$ denotes nearest neighbors within block $\mathbf{b}_{ij}$ in the horizontal (x) and vertical (y) direction, respectively.

Interblock defects. Finally, we define the fraction of interblock defects between neighboring blocks in the horizontal and vertical direction, respectively, given by

$$\xi_{ij}^{x\pm}(\{\mathbf{b}_{ij}, \mathbf{b}_{i\pm1\,j}\}) \equiv \left(z_x N_\sigma^b\right)^{-1} \sum_{\langle mn,kl\rangle_x \in (\mathbf{b}_{ij}, \mathbf{b}_{i\pm1\,j})} |\sigma_{mn} - \sigma_{kl}|,$$
$$\xi_{ij}^{y\pm}(\{\mathbf{b}_{ij}, \mathbf{b}_{ij\pm1}\}) \equiv \left(z_y N_\sigma^b\right)^{-1} \sum_{\langle mn,kl\rangle_y \in (\mathbf{b}_{ij}, \mathbf{b}_{ij\pm1})} |\sigma_{mn} - \sigma_{kl}|, \tag{12}$$

where one needs to account for the boundary conditions upon summing over boundary blocks.

As an example, the fraction of down spins, intrablock defects, and interblock defects for the lower left block in Fig. 3(b) under periodic boundary conditions is $\varphi_{11} = 1/4$, $\zeta_{11}^{x,y} = 1/8$, $\xi_{11}^{x+} = 1/8$, $\xi_{11}^{x-} = 1/4$, $\xi_{11}^{y+} = 0$, and $\xi_{11}^{y-} = 1/8$.

C. Coarse-grained Ising Hamiltonian

We now rewrite the nearest-neighbor Ising Hamiltonian in terms of the coarse-grained intensive lattice observables introduced in Eqs. (11) and (12). The Ising Hamiltonian reads as (in units of $k_\mathrm{B}T$)

$$\mathcal{H}(\boldsymbol{\sigma}) = -J_x \sum_{\langle mn,kl\rangle_x} \sigma_{mn}\sigma_{kl} - J_y \sum_{\langle mn,kl\rangle_y} \sigma_{mn}\sigma_{kl}, \tag{13}$$

where $\boldsymbol{\sigma}$ is the matrix containing all spin configurations, and $J_{x,y} \geqslant 0$ is the ferromagnetic interaction strength in the horizontal and vertical direction, respectively. To make use of Eqs. (11) and (12) we insert the identities

$$\sigma_{mn}\sigma_{kl} = 1 - |\sigma_{mn} - \sigma_{kl}|,$$
$$\sum_{\langle mn,kl\rangle_{x,y}} 1 = z_{x,y} N_\sigma^{x,y}/2$$

(the latter can also be read as a definition for $z_{x,y}$) and decompose the Hamiltonian into a sum over interblock and intrablock contributions

$$\mathcal{H}(\boldsymbol{\sigma}) = N_\sigma^b \sum_{i=1}^{N_b^x} \sum_{j=1}^{N_b^y} [\mathcal{H}_{\mathrm{inter}} + \mathcal{H}_{\mathrm{intra}} - \mathcal{C}]. \tag{14}$$

The respective contributions inside the sum are given by

$$\mathcal{H}_{\text{inter}}(\{\mathbf{b}_{i\pm1j},\mathbf{b}_{ij},\mathbf{b}_{ij\pm1}\}) = z_x J_x\big(\xi_{ij}^{x+}+\xi_{ij}^{x-}\big)/2+(x\leftrightarrow y),$$
$$\mathcal{H}_{\text{intra}}(\{\mathbf{b}_{ij}\}) = z_x J_x \zeta_{ij}^{x} + (x \leftrightarrow y), \tag{15}$$
$$\mathcal{C} = (z_x J_x + z_y J_y)/2.$$

The term $(x \leftrightarrow y)$ in Eq. (15) denotes a repetition of the preceding term with x and y interchanged. Equation (14) is an *exact* expression for the Ising Hamiltonian in terms of spin blocks. Note that the factor $1/2$ in $\mathcal{H}_{\text{inter}}$ accounts for the double counting over interblock contributions.

D. Coarse-grained partition function

Since the Hamiltonian is decomposed into a sum over spin blocks, the partition function Z can be factorized into a product of partition functions per block $\mathcal{Z}_{ij}$. Inserting Eq. (14) into the partition function leads to the following *exact* expression:

$$Z = \prod_{i=1}^{N_b^x}\prod_{j=1}^{N_b^y}\mathcal{Z}_{ij} \equiv \prod_{i=1}^{N_b^x}\prod_{j=1}^{N_b^y}\sum_{\{\mathbf{b}_{ij}\}} \mathrm{e}^{-N_\sigma^b[\mathcal{H}_{\text{inter}}+\mathcal{H}_{\text{intra}}-\mathcal{C}]}. \tag{16}$$

The evaluation of the configurational sum over all possible spin-block configurations $\{\mathbf{b}_{ij}\}$ constitutes a difficult, if not impossible, task. However, the Hamiltonian given by Eq. (15) solely depends on the seven lattice observables $(\varphi_{ij}, \zeta_{ij}^{x,y}, \xi_{ij}^{x,y\pm})$. Therefore, we can interchange the configurational sum by a sum over all possible values of these seven lattice observables, and introduce a *degeneracy of states* $\Psi(\varphi_{ij}, \zeta_{ij}^{x,y}, \xi_{ij}^{x,y\pm})$, which accounts for the multiplicity of configurations. Then we obtain

$$\mathcal{Z}_{ij} = \sum_{\varphi_{ij}}\sum_{\zeta_{ij}^{x,y}}\sum_{\xi_{ij}^{x,y\pm}} \Psi\big(\varphi_{ij}, \zeta_{ij}^{x,y}, \xi_{ij}^{x,y\pm}\big)\mathrm{e}^{-N_\sigma^b[\mathcal{H}_{\text{inter}}+\mathcal{H}_{\text{intra}}-\mathcal{C}]}. \tag{17}$$

Equation (17) is an exact expression as long as the degeneracy of states $\Psi(\varphi_{ij}, \zeta_{ij}^{x,y}, \xi_{ij}^{x,y\pm})$ is evaluated exactly.

Normalization condition. For $(J_x, J_y) = (0, 0)$ the degeneracy of states should obey the relation

$$\sum_{\zeta_{ij}^{x,y}}\sum_{\xi_{ij}^{x,y\pm}} \Psi\big(\varphi_{ij}, \zeta_{ij}^{x,y}, \xi_{ij}^{x,y\pm}\big) \overset{!}{=} \binom{N_\sigma^b}{\varphi_{ij}N_\sigma^b} \tag{18}$$

since this is the number of possible configurations to place $\varphi_{ij}N_\sigma^b$ down spins in a block that contains N_σ^b spins in total. We will use Eq. (18) as a normalization condition to consistently approximate the degeneracy of states.

E. Pair-approximation ansatz

Intuition behind the BG approximation. Our next aim is to approximate the degeneracy of states *by placing spin pairs onto the lattice*. Imagine that we are given a number of spin pairs with $N_{\uparrow\uparrow}$, $N_{\downarrow\downarrow}$, and $N_{\uparrow\downarrow}$ denoting the number of up-up, down-down, and up-down (i.e., defects) spin pairs. The total number of distinct lattice configurations for fixed $(N_{\uparrow\uparrow}, N_{\downarrow\downarrow}, N_{\uparrow\downarrow})$ is given by [75]

$$\Psi \approx \Psi_{\text{BG}} \equiv \frac{(N_{\uparrow\uparrow}+N_{\uparrow\downarrow}+N_{\downarrow\downarrow})!}{(N_{\uparrow\uparrow})!(N_{\uparrow\downarrow}/2)!^2(N_{\downarrow\downarrow})!},$$

where the factor $1/2$ in the denominator accounts for the symmetry $N_{\uparrow\downarrow} = N_{\downarrow\uparrow}$. For even $N_{\uparrow\downarrow}$ the term $(N_{\uparrow\downarrow}/2)!$ is well defined. However, when $N_{\uparrow\downarrow}$ is odd we are forced to consider the generalized factorial

$$\Psi \approx \Psi_{\text{BG}} \equiv \frac{\Gamma(N_{\uparrow\uparrow}+N_{\uparrow\downarrow}+N_{\downarrow\downarrow}+1)}{\Gamma(N_{\uparrow\uparrow}+1)\Gamma(N_{\uparrow\downarrow}/2+1)^2\Gamma(N_{\downarrow\downarrow}+1)}, \tag{19}$$

where $\Gamma(x)$ is the gamma function [76]. Equation (19) comprises the main essence of the BG approximation.[1]

Nonuniform degeneracy of states. To account for a nonuniform concentration profile we need to construct the degeneracy of states for each of the individual blocks $\mathbf{b}_{ij}$. Similar to Eq. (19) we introduce a pair-approximation ansatz for the degeneracy of states. The difference, however, is that we now distinguish between intrablock and interblock contributions. Furthermore, we want to express the degeneracy of states in terms of Eqs. (10)–(12). This results in

$$\Psi\big(\varphi_{ij}, \zeta_{ij}^{x,y}, \xi_{ij}^{x,y\pm}\big) \approx \mathcal{N}(\varphi_{ij})\hat{\Psi}\big(\varphi_{ij}, \zeta_{ij}^{x,y}, \xi_{ij}^{x,y\pm}\big), \tag{20}$$

where $\mathcal{N}(\varphi_{ij})$ is a normalization constant left to be determined. The unnormalized degeneracy of states reads as

$$\hat{\Psi} \equiv \hat{\Psi}_{\text{intra}}^{-\frac{1}{2}}\big(\varphi_{ij}, \zeta_{ij}^{x,y}\big)\prod_{\pm}\hat{\Psi}_{\text{inter}}^{-\frac{1}{4}}\big(\varphi_{ij}, \xi_{ij}^{x,y\pm}\big), \tag{21}$$

which is divided into intrablock and interblock contributions

$$\hat{\Psi}_{\text{intra}} \equiv \psi_x\big(\varphi_{ij}, \varphi_{ij}, \zeta_{ij}^{x}\big)\psi_y\big(\varphi_{ij}, \varphi_{ij}, \zeta_{ij}^{y}\big), \tag{22}$$
$$\hat{\Psi}_{\text{inter}} \equiv \psi_x\big(\varphi_{ij}, \varphi_{i\pm1j}, \xi_{ij}^{x\pm}\big)\psi_y\big(\varphi_{ij}, \varphi_{ij\pm1}, \xi_{ij}^{y\pm}\big), \tag{23}$$

and the auxiliary functions $\psi_{x,y}(a, b, c)$ are given by

$$\psi_{x,y}(a,b,c) \equiv \hat{\Gamma}_{x,y}(1-a-c)\hat{\Gamma}_{x,y}(b-c) \times \hat{\Gamma}_{x,y}(a-b+c)\hat{\Gamma}_{x,y}(c),$$

with $\hat{\Gamma}_{x,y}(w) \equiv \Gamma(z_{x,y}N_\sigma^b w/2+1)$, and $\Gamma(w)$ being the gamma function. Equation (20) can be derived similarly to Eq. (19) by counting the number of degenerate configurations upon distributing spin pairs over a lattice. The functions $\psi_{x,y}(\varphi_{ij}, \varphi_{ij}, \zeta_{ij}^{x,y})$ account for distributing spin pairs inside a single block in the horizontal and vertical direction, respectively. Similarly, $\psi_x(\varphi_{ij}, \varphi_{i\pm1j}, \xi_{ij}^{x\pm})$ and $\psi_y(\varphi_{ij}, \varphi_{ij\pm1}, \xi_{ij}^{y\pm})$ account for distributing spin pairs between two neighboring blocks in the horizontal and vertical direction, respectively.

F. Evaluation of normalization constant

The normalization constant $\mathcal{N}(\varphi_{ij})$ in Eq. (20) is determined by Eq. (18). To evaluate the six sums over the lattice observables $(\zeta_{ij}^{x,y}, \xi_{ij}^{x,y\pm})$ we take the thermodynamic limit of the spins, rendering the observables continuous, and employ the maximum term method (i.e., saddle-point approximation). This gives the following maximizing arguments (henceforth

[1] Equation (19) is exact when there are no closed loops in the lattice. Therefore, the BG approximation is exact on the Bethe lattice.

indicated with a hat):

$$\begin{aligned}
\hat{\zeta}^{x,y}(\varphi_{ij}) &\equiv \arg\sup_{\zeta_{ij}^{x,y}} \left\{\lim_{\mathrm{s}}^{\mathbf{N}_\sigma}\left[\left(N_\sigma^b\right)^{-1}\ln\left[\psi_{x,y}^{-\frac{1}{2}}\left(\varphi_{ij},\varphi_{ij},\zeta_{ij}^{x,y}\right)\right]\right]\right\} = \varphi_{ij}(1-\varphi_{ij}),\\
\hat{\xi}^{x\pm}(\varphi_{i\pm1j},\varphi_{ij}) &\equiv \arg\sup_{\xi_{ij}^{x\pm}} \left\{\lim_{\mathrm{s}}^{\mathbf{N}_\sigma}\left[\left(N_\sigma^b\right)^{-1}\ln\left[\psi_{x}^{-\frac{1}{4}}\left(\varphi_{ij},\varphi_{i\pm1j},\xi_{ij}^{x\pm}\right)\right]\right]\right\} = \varphi_{i\pm1j}(1-\varphi_{ij}),\\
\hat{\xi}^{y\pm}(\varphi_{ij\pm1},\varphi_{ij}) &\equiv \arg\sup_{\xi_{ij}^{y\pm}} \left\{\lim_{\mathrm{s}}^{\mathbf{N}_\sigma}\left[\left(N_\sigma^b\right)^{-1}\ln\left[\psi_{y}^{-\frac{1}{4}}\left(\varphi_{ij},\varphi_{ij\pm1},\xi_{ij}^{y\pm}\right)\right]\right]\right\} = \varphi_{ij\pm1}(1-\varphi_{ij}).
\end{aligned} \tag{24}$$

To obtain Eq. (24) we used Stirling's approximation for the gamma function $\ln\Gamma(x) = \Xi(x) - x + O(\ln x)$ for $\mathrm{Re}(x) > 0$ with $\Xi(x) \equiv x\,\ln(x)$. Plugging Eq. (24) into Eq. (20), and finally solving Eq. (18) for the normalization constant yields

$$\mathcal{N}(\varphi_{ij}) = \binom{N_\sigma^b}{\varphi_{ij}N_\sigma^b}\hat{\Psi}^{-1}(\varphi_{ij},\hat{\zeta}^{x,y},\hat{\xi}^{x,y\pm}).$$

G. Evaluation of partition function

With the normalization constant evaluated explicitly, we can now determine the partition function given by Eq. (17) in combination with (20). Again, we take the thermodynamic limit of the spins and approximate the six inner sums over $(\zeta_{ij}^{x,y}, \xi_{ij}^{x,y\pm})$ in Eq. (17) with the maximum term method, giving the following extremizing arguments (henceforth indicated with a hat + dagger †):

$$\begin{aligned}
\hat{\zeta}_\dagger^{x,y}(\varphi_{ij}) &\equiv \arg\sup_{\zeta_{ij}^{x,y}} \left\{\lim_{\mathrm{s}}^{\mathbf{N}_\sigma}\left[\left(N_\sigma^b\right)^{-1}\ln\left[\psi_{x,y}^{-\frac{1}{2}}\left(\varphi_{ij},\varphi_{ij},\zeta_{ij}^{x,y}\right)\mathrm{e}^{-z_{x,y}J_{x,y}\zeta_{ij}^{x,y}N_\sigma^b}\right]\right]\right\} = 2\hat{\zeta}^{x,y}/\Omega_{x,y}(0,\hat{\zeta}^{x,y}),\\
\hat{\xi}_\dagger^{x\pm}(\varphi_{i\pm1j},\varphi_{ij}) &\equiv \arg\sup_{\xi_{ij}^{x\pm}} \left\{\lim_{\mathrm{s}}^{\mathbf{N}_\sigma}\left[\left(N_\sigma^b\right)^{-1}\ln\left[\psi_{x}^{-\frac{1}{4}}\left(\varphi_{ij},\varphi_{i\pm1j},\xi_{ij}^{x\pm}\right)\mathrm{e}^{-z_xJ_x\xi_{ij}^{x\pm}N_\sigma^b/2}\right]\right]\right\} = 2\hat{\xi}^{x\pm}/\Omega_x(\varphi_{ij}-\varphi_{i\pm1j},\hat{\xi}^{x\pm}),\\
\hat{\xi}_\dagger^{y\pm}(\varphi_{ij\pm1},\varphi_{ij}) &\equiv \arg\sup_{\xi_{ij}^{y\pm}} \left\{\lim_{\mathrm{s}}^{\mathbf{N}_\sigma}\left[\left(N_\sigma^b\right)^{-1}\ln\left[\psi_{y}^{-\frac{1}{4}}\left(\varphi_{ij},\varphi_{ij\pm1},\xi_{ij}^{y\pm}\right)\mathrm{e}^{-z_yJ_y\xi_{ij}^{y\pm}N_\sigma^b/2}\right]\right]\right\} = 2\hat{\xi}^{y\pm}/\Omega_y(\varphi_{ij}-\varphi_{ij\pm1},\hat{\xi}^{y\pm}),
\end{aligned} \tag{25}$$

where we introduced the auxiliary function

$$\Omega_{x,y}(a,b) \equiv 1 + a\gamma_{x,y} + [\delta_{a,0}+\mathrm{sgn}(a)]([1+a\gamma_{x,y}]^2 + 4b\gamma_{x,y})^{\frac{1}{2}},$$

with $\mathrm{sgn}(x) = \pm 1$ for $\pm x > 0$, $\mathrm{sgn}(0) = 0$, and $\gamma_{x,y} \equiv \mathrm{e}^{4J_{x,y}} - 1$. For $(J_x, J_y) = (0,0)$ we have $\hat{\zeta}_\dagger^{x,y} = \hat{\zeta}^{x,y}$ and $\hat{\xi}_\dagger^{x,y\pm} = \hat{\xi}^{x,y\pm}$, as expected from their definition. With the six inner sums in Eq. (17) evaluated, we are left with the sum over φ_{ij}. To evaluate the last sum we introduce the *free-energy density* in the thermodynamic limit of the spins

$$\begin{aligned}
&\mathrm{f}(\varphi_{i\pm1j},\varphi_{ij},\varphi_{ij\pm1})\\
&\equiv \lim_{\mathrm{s}}^{\mathbf{N}_\sigma}\left[-\left(N_\sigma^b\right)^{-1}\ln\left(\Psi(\varphi_{ij},\hat{\zeta}_\dagger^{x,y},\hat{\xi}_\dagger^{x,y\pm})\mathrm{e}^{-N_\sigma^b[z_xJ_x(\hat{\zeta}_\dagger^x+\{\hat{\xi}_\dagger^{x+}+\hat{\xi}_\dagger^{x-}\}/2)+(x\leftrightarrow y)-\mathcal{C}]}\right)\right]\\
&= (z_x/8)\sum_{\pm}[\Xi(1-\varphi_{ij}-\hat{\xi}_\dagger^{x\pm}) + \Xi(\varphi_{i\pm1j}-\hat{\xi}_\dagger^{x\pm}) + \Xi(\varphi_{ij}-\varphi_{i\pm1j}+\hat{\xi}_\dagger^{x\pm}) + \Xi(\hat{\xi}_\dagger^{x\pm}) - \Xi(1-\varphi_{i\pm1j}) - \Xi(\varphi_{i\pm1j})]\\
&\quad + (z_y/8)\sum_{\pm}[\Xi(1-\varphi_{ij}-\hat{\xi}_\dagger^{y\pm}) + \Xi(\varphi_{ij\pm1}-\hat{\xi}_\dagger^{y\pm}) + \Xi(\varphi_{ij}-\varphi_{ij\pm1}+\hat{\xi}_\dagger^{y\pm}) + \Xi(\hat{\xi}_\dagger^{y\pm}) - \Xi(1-\varphi_{ij\pm1}) - \Xi(\varphi_{ij\pm1})]\\
&\quad + \{(z_x/4)[\Xi(1-\varphi_{ij}-\hat{\zeta}_\dagger^x) + \Xi(\varphi_{ij}-\hat{\zeta}_\dagger^x) + 2\Xi(\hat{\zeta}_\dagger^x)] + (x\leftrightarrow y)\} + (1-3z/4)[\Xi(\varphi_{ij}) + \Xi(1-\varphi_{ij})]\\
&\quad + \{z_xJ_x(\hat{\zeta}_\dagger^x + \{\hat{\xi}_\dagger^{x+} + \hat{\xi}_\dagger^{x-}\}/2) + (x\leftrightarrow y)\} - \mathcal{C},
\end{aligned} \tag{26}$$

where $(x \leftrightarrow y)$ always applies directly to its preceding term, and we recall that $\Xi(x) \equiv x\,\ln(x)$. To optimize Eq. (26) over φ_{ij}, we can employ two different strategies:

(1) Optimize $\mathrm{f}(\varphi_{i\pm1j},\varphi_{ij},\varphi_{ij\pm1})$ and apply $\lim_{\mathrm{s}}^{\mathbf{N}_b}[\cdot]$.

(2) Take $\lim_{\mathrm{s}}^{\mathbf{N}_b}[\mathrm{f}(\varphi_{i\pm1j},\varphi_{ij},\varphi_{ij\pm1})]$ and then optimize.

In Appendix C 2 we apply the first strategy, and here we proceed with the second. Upon evaluating the thermodynamic limit of the blocks in Eq. (26) we need to keep track of various terms, which is done explicitly in Appendix C 3. Here we fastforward to the final result. Restoring the product over the spin blocks in Eq. (16), and expressing $\mathbf{x}$ in units of the block lengths (l_x, l_y), we obtain

$$F \equiv \lim_{\mathrm{s}}^{\mathbf{N}_b}\left[(N_b)^{-1}\sum_{i=1}^{N_b^x}\sum_{j=1}^{N_b^y}\mathrm{f}(\varphi_{i\pm1j},\varphi_{ij},\varphi_{ij\pm1})\right] = \int_A d\mathbf{x}\left[\mathrm{f}(\varphi(\mathbf{x})) + \frac{1}{2}\nabla\varphi(\mathbf{x})^T\boldsymbol{\kappa}(\varphi(\mathbf{x}))\nabla\varphi(\mathbf{x})\right], \tag{27}$$

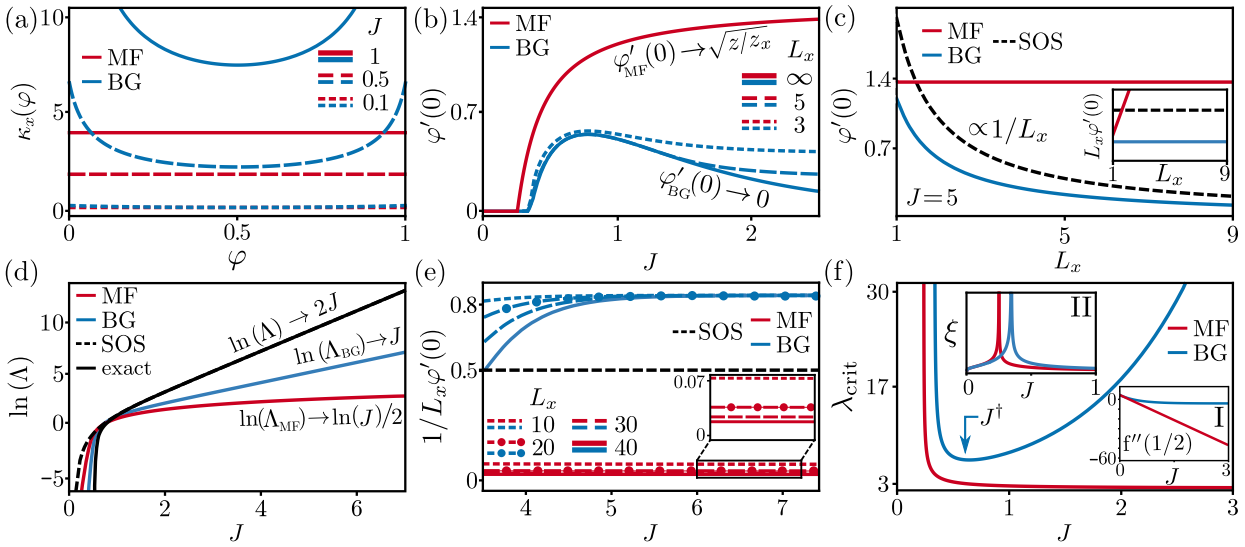

FIG. 4. In all panels we consider a square-lattice Ising strip with $\{z_x, z_y\} = \{2, 2\}$. Red, blue, and black solid and dashed lines correspond to MF, BG, and exact and SOS results, respectively. (a) x component of the gradient-energy coefficient κ_x, given by Eq. (29) as a function of φ for $J \in \{0.1, 0.5, 1\}$. (b), (c) Interface steepness $\varphi'(0) = \partial_x\varphi|_{x=0}$ of the equilibrium concentration profile as a function of J for fixed $L_x \in \{3, 5, \infty\}$ (b), and as a function of L_x for fixed $J = 5$ (c). Inset of (c): rescaled steepness $L_x\varphi'(0)$. (d) Interface stiffness Λ defined in Eq. (32) as a function of J on a logarithmic scale. The exact result (black line) is given by Eq. (1). (e) $1/L_x\varphi'(0)$ as a function of J for fixed $L_x \in \{10, 20, 30, 40\}$. Blue lines converge to the value $\Delta_{\rm BG} \approx 0.835$, corresponding to the instantaneous interface width [see also Eq. (35)]. Inset: blowup of the MF result. (f) Critical stability wavelength $\lambda_{\rm crit} = 2\pi[-\kappa_x(1/2)/f''(1/2)]^{1/2}$ as a function of J; the blue arrow indicates $J^\dagger$ in Eq. (37) where $\lambda_{\rm crit}$ attains a minimum. Inset I: curvature of the free-energy barrier $f''(1/2)$. Inset II: bulk correlation length ξ defined in Eq. (38).

where $A = [-L_x/2, L_x/2] \times [-L_y/2, L_y/2]$, and the *local free-energy density* $f(\varphi)$ and concentration-dependent *gradient-energy coefficient* $\boldsymbol{\kappa}(\varphi)$ are given by

$$\begin{aligned} f(\varphi) = {} & 2[z_xJ_x\hat{\xi}^x_\dagger + z_yJ_y\hat{\xi}^y_\dagger - 1/4] \\ & + (1-z)[\Xi(\varphi) + \Xi(1-\varphi)] \\ & + (z_x/2)[\Xi(\varphi-\hat{\xi}^x_\dagger) + \Xi(1-\varphi-\hat{\xi}^x_\dagger) + 2\Xi(\hat{\xi}^x_\dagger)] \\ & + (x \leftrightarrow y), \end{aligned} \tag{28}$$

$$\boldsymbol{\kappa}(\varphi) = \frac{\mathbf{z}(\exp 4\mathbf{J} - 1)}{4[1 + 4(\exp 4\mathbf{J} - 1)\varphi(1-\varphi)]^{1/2}}, \tag{29}$$

with $\mathbf{J} = \mathrm{diag}(J_x, J_y)$. Equations (27)–(29) are the main result of the theoretical work presented here. The MF analogs are obtained by taking the weak interaction limit $\lim_{J_{x,y}\to 0} f(\varphi) = f_{\rm MF}(\varphi) + O(J^2_{x,y})$ where $f_{\rm MF}(\varphi)$ is given by Eq. (B10), and $\lim_{J_{x,y}\to 0} \boldsymbol{\kappa}(\varphi) = \boldsymbol{\kappa}_{\rm MF} + O(J^2_{x,y})$ with $\boldsymbol{\kappa}_{\rm MF} = \mathbf{zJ}$. Similarly, $f_{\rm MF}(\varphi)$ can be obtained with the substitution $\hat{\xi}^{x,y}_\dagger \to \hat{\xi}^{x,y}$ in Eq. (28). Note that $\boldsymbol{\kappa}_{\rm MF}$ is independent of φ, in agreement with regular solution theory [1]. Figure 4(a) displays κ_x as a function of φ for BG and MF theory (blue and red lines, respectively). Here we observe a large *entropic* penalty of inhomogeneities at $\varphi \to \{0, 1\}$ *not* accounted for in MF theory.

VI. ANALYSIS OF FREE-ENERGY FUNCTIONAL ACCOUNTING FOR PAIR CORRELATIONS

A. Equilibrium interface profile

In subsequent analysis we consider an isotropic interaction strength $J_x = J_y = J$. The equilibrium profile minimizes F, i.e., it is the solution of $\delta F/\delta\varphi(\mathbf{x}) = 0$. We now show that BG and MF theories predict starkly different behavior for moderate and strong interactions: MF theory fails to account for the interface broadening explained in Sec. II. First, considering Fig. 1, we focus on the square-lattice Ising strip ($L_y \gg L_x$) where the magnetization varies only in the x direction, i.e., $\varphi(\mathbf{x}) = \varphi(x)$. The profile is obtained as the solution of a nonlinear second-order differential equation [see Eq. (C9)] that we solve numerically. The boundary conditions are given by $\varphi(-L_x/2) = \varphi_{\rm min}$ and $\varphi(L_x/2) = 1 - \varphi_{\rm min}$, where

$$\varphi_{\rm min} \equiv \arg \inf_{0<\varphi\leqslant 1/2} f(\varphi) \tag{30}$$

is the coexisting state determined by the location of the left minimum of $f(\varphi)$. Note that $f(\varphi)$ is mirror symmetric around $\varphi = 1/2$ in the absence of an external field. Above the critical coupling $J > J_{\rm crit}$, where [77]

$$J_{\rm BG,crit} \equiv \ln(z/[z-2])/2, \quad J_{\rm MF,crit} \equiv 1/z,$$

$f(\varphi)$ has two local minima resulting in a nonuniform $\varphi(x)$. For $J \leqslant J_{\rm crit}$ the profile is uniform. We fix the ensemble interface location such that $\varphi(0) = 1/2$.[2]

Qualitative differences between the profiles predicted by BG and MF theory are seen already in Figs. 1(c) and 1(d). In particular, BG concentration profiles depend nonmonotonically on J, which is confirmed by Monte Carlo (MC)

[2]Fixing the ensemble-averaged interface position is not equal to fixing the position of instantaneous profiles. Thus, the interface location along individual trajectories may still fluctuate.

simulations of the Ising model (for simulation details see Appendix A), whereas MF interfaces become monotonically steeper. By comparing with Fig. 1(b) we observe that interface broadening correlates with interface delocalization. This is further analyzed systematically in Fig. 4.

First, we inspect in Fig. 4(b) the interface steepness $\varphi'(0)$. In stark contrast to MF theory predicting a steepening interface independent of lattice size L_x, BG profiles are nonmonotonic in J beyond a sufficient L_x due to interface delocalization. To verify that this is *no* artifact, we compare our results with the *solid-on-solid* (SOS) model for the square-lattice Ising strip ($z = 4$), which becomes exact in the limit $J \to \infty$, and is known to include interface delocalization [60–64]. The SOS model yields [61,62,64]

$$\lim_{J\to\infty} \varphi_{\rm SOS}(x) = 1/2 + x/L_x + \sin(2\pi x/L_x)/2\pi, \tag{31}$$

hence, $\lim_{J\to\infty} \varphi'_{\rm SOS}(0) = 2/L_x$. In Fig. 4(c) we show the interface steepness as a function of L_x for fixed J, and find that the SOS and BG results display the same scaling with respect to L_x [see Fig. 4(c) inset], whereas the MF result is in fact independent of L_x.

Further verification is given by the interface stiffness, which is the free-energy difference between the nonuniform equilibrium profile $\varphi(x)$ and a uniform equilibrium profile $\varphi_{\rm min}$, and reads as [see Eq. (2.15) in [1]]

$$\Lambda \equiv 2\int_{\varphi_{\rm min}}^{1-\varphi_{\rm min}} \{\kappa(\varphi)[{\rm f}(\varphi) - {\rm f}(\varphi_{\rm min})]\}^{1/2} d\varphi, \tag{32}$$

which is depicted in Fig. 4(d). Note that surface tension is related to surface stiffness via $\sigma = \operatorname{arcsinh}(\Lambda)$ [61]. The exact result is given by Eq. (1), while the SOS model yields $\Lambda_{\rm SOS} = \cosh(2J) - 1$ [61], and converges to the exact result for large J, i.e., $\lim_{J\to\infty} \ln(\Lambda_{\rm SOS}) \simeq 2J$. Notably, the BG result is considerably more accurate than the MF prediction [compare blue and red lines with the black line in Fig. 4(d), and also displays a correct exponential scaling, $\lim_{J\to\infty} \ln(\Lambda_{\rm BG}) \simeq J$, in stark contrast to the square-root MF scaling $\lim_{J\to\infty} \ln(\Lambda_{\rm MF}) \simeq \ln(\sqrt{J})$.

B. Disentangling interface delocalization

By exploiting the mapping of instantaneous interface positions onto a Brownian excursion problem (see Sec. IV) we can disentangle interface delocalization from the instantaneous interface width Δ in the large-J limit where the instantaneous interface positions become asymptotically uniformly distributed, i.e.,

$$\lim_{J\to\infty} p_{\rm int}(x; J) = L_x^{-1} \mathbb{1}_{|x|<L_x/2}, \tag{33}$$

with $\mathbb{1}_{|x|<L_x/2}$ equal to 1 when $|x|<L_x/2$ and 0 otherwise (see derivation in Sec. IV C). Let us assume that for $J \gg 1$ each instantaneous profile $\varphi_j(x)$ is given by some continuous function $f(x/\Delta + b_j) : \mathbb{R} \to [0, 1]$ obeying $\lim_{x\to\pm\infty} f(x) = (1 \pm 1)/2$, where $\Delta > 0$ and b_j describe the width and position of the jth instantaneous interface. The ensemble-averaged profile is then given by the convolution of $f(x)$ with the probability density to have a certain shift b, i.e.,

$$\lim_{J\to\infty} \varphi(x) = L_x^{-1} \int f(x/\Delta + b)\mathbb{1}_{|b|<L_x/2} db. \tag{34}$$

We can now compute the interface steepness and find $\lim_{J\to\infty} L_x\varphi'(0) = \Delta^{-1}[f(L_x/2) - f(-L_x/2)]$. Finally, taking the large-L_x limit, we obtain

$$\lim_{L_x\to\infty} \lim_{J\to\infty} 1/L_x\varphi'(0) = \Delta, \tag{35}$$

which thereby disentangles interface delocalization from the instantaneous interface width Δ. For the Ising strip this yields $\Delta_{\rm SOS} = 0.5$ within the SOS model obtained from Eq. (31), and $\Delta_{\rm BG} \approx 0.835$ with the BG approximation [see Fig. 4(e)]. Hence, while the ensemble-averaged steepness vanishes in the large coupling limit due to interface delocalization, instantaneous realizations maintain a nonzero interface steepness with uniformly distributed interface positions. Importantly, MF theory does *not* account for delocalization-induced interface broadening and therefore predicts $\Delta_{\rm MF} \to 0$ [see inset of Fig. 4(e)].

C. Spinodal decomposition

Having established the physical consistency of Eqs. (27)–(29), we now address phase separation, and determine the length scales on which inhomogeneities are stable by performing a linear stability analysis on the total free-energy density around a uniform concentration profile, i.e., $\varphi(x) = \varphi_0 + a\sin(qx)$ with $|a| \ll \min(\varphi_0, 1 - \varphi_0)$ (the symmetry of the problem imposes odd inhomogeneities). Stable perturbations lower the total free-energy density $\Delta F \equiv F[\varphi(x)] - F[\varphi_0] \leqslant 0$, yielding an upper bound on stable wave vectors $q \leqslant q_{\rm crit}$ with the critical wave vector given by (see Appendix E)

$$q_{\rm crit} \equiv \sqrt{-{\rm f}''(\varphi_0)/\kappa_x(\varphi_0)} = \sqrt{\frac{2(z-2)[1 + 4(e^{4J}-1)\varphi_0(1-\varphi_0)]^{\frac{1}{2}} - 2z}{z_x\varphi_0(1-\varphi_0)(e^{4J}-1)}}, \tag{36}$$

where ${\rm f}''(\varphi_0) = d^2{\rm f}(\varphi)/d\varphi^2|_{\varphi=\varphi_0}$ is the curvature of the free-energy barrier. The critical wave vector translates into a critical wavelength $\lambda_{\rm crit} = 2\pi/q_{\rm crit}$, above which perturbations are stable. Figure 4(f) depicts $\lambda_{\rm crit}$ for a square lattice with $\varphi_0 = 1/2$ as a function of J. Similar to the results shown in Fig. 4(b), $\lambda_{\rm crit}$ displays a nonmonotonic trend within BG theory (blue lines)[3] that is contrasted by a monotonic attenuation in the MF theory (red lines). The interaction strength minimizing $\lambda_{\rm crit}$ in the BG theory, i.e., the interaction strength J allowing for the widest range of stable wavelengths, can be determined exactly and reads as [see blue arrow in Fig. 4(f)]

$$J^\dagger(\varphi_0) = \frac{1}{4}\ln\left(1 + \frac{z(2+\sqrt{z-1}) - 2}{(z-2)^2\varphi_0(1-\varphi_0)}\right), \tag{37}$$

with the corresponding $\lambda_{\rm crit}^{\rm min} \equiv \lambda_{\rm crit}(J^\dagger)$ given by the reciprocal of Eq. (E8). The nonmonotonicity of $\lambda_{\rm crit}$ can be understood by inspecting how the curvature of the barrier depends on J. In particular, the BG curvature converges, $\lim_{J\to\infty} {\rm f}''(1/2) = 2(2-z)$ [see Fig. 4(f), inset I], whereas

[3]The nonmonotonic dependence of $\lambda_{\rm crit}^{\rm BG}$ on J in fact persists for any background concentration $0 < \varphi_0 < 1$ [see Fig. 8(c)].

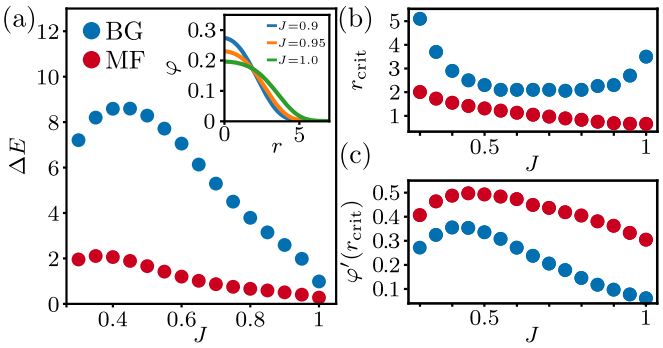

FIG. 5. Numerical simulations of critical nuclei of the radially symmetric Cahn-Hilliard equation with the BG (blue) and MF (red) free energy for a hexagonal coordination $\{z, z_x\} = \{6, 4\}$. (a) Free-energy difference ΔE between the critical nucleus and the homogeneous state as a function of the interaction strength J. The inset shows critical profiles $\varphi(r)$ for three values of J. (b) Radius $r_{\rm crit}$ and (c) interface steepness $\varphi'(r_{\rm crit})$ of the critical nucleus as a function of J.

the free-energy penalty of inhomogeneities increases exponentially, eventually increasing $\lambda_{\rm crit}$. MF overestimates the curvature of the barrier, and underestimates the free-energy penalty of inhomogeneities, leading a decrease in $\lambda_{\rm crit}^{\rm MF}$. Notably, the bulk correlation length

$$\xi \equiv \sqrt{\kappa_x(\varphi_{\rm min})/{\rm f}''(\varphi_{\rm min})} \tag{38}$$

[41] displays qualitatively the same behavior in both theories [see Fig. 4(f), inset II] since the MF free-energy density is relatively accurate near the local minimum $\varphi_{\rm min}$, but inaccurate near the barrier (see Appendix F and [77]).

D. Implications for nucleation

We next investigate, in Fig. 5, how interface broadening affects nucleation, by determining minimal free-energy paths (the reaction coordinate and method are described in Appendix G). The inset in Fig. 5(a) suggests that critical nuclei become less dense and wider as J becomes larger. Indeed, we find that correlations captured by BG theory lead to larger critical nuclei [Fig. 5(b)], shallower interfaces [Fig. 5(c)], and that the increasing trend with J is only captured by BG theory, which is reminiscent of the results shown in Fig. 4. Most importantly, BG theory predicts that the nucleation barrier ΔE is approximately four times larger than predicted by MF [Fig. 5(a)], implying a strong reduction of nucleation rates [78–81].

To understand why interface delocalization affects nucleation we note that shifting the interface position corresponds to a growing or shrinking nucleus which alters the free energy. Instantaneous interfaces are still affected by interface translation and capillary-wave fluctuations. However, in contrast to the strip, distinct instantaneous interface configurations are *not* isoenergetic. The weighting by the respective free energy of the configuration ultimately gives rise to broadening, and thus larger critical nuclei and higher nucleation barriers.

VII. CONCLUSION

By directly computing the thermodynamic limit of a spatially inhomogeneous Ising model on general lattices within the Bethe-Guggenheim approximation we derived a Cahn-Hilliard–type phase-field free energy that accounts for nearest-neighbor pair correlations. Strong interactions were shown to give rise to (i) a delocalization-induced interface broadening confirmed by exact results for the two-dimensional Ising model, (ii) a strong reduction of nucleation kinetics due to an amplification of the free-energy barrier to nucleation, and (iii) a nonmonotonic dependence of critical nucleus size on interaction strength. These effects are the result of an entropy-driven interplay between capillary-wave and interface-position fluctuations at sufficiently strong coupling, and pair correlations are required to correctly account for them. Pair correlations enforce a thermodynamically optimal configuration of defects, and are thus an essential determinant of interfaces and condensates in the strong interaction limit that so far have been overlooked. By neglecting correlations, mean-field reasoning inherently disregards correlations and thus cannot account for local defects and their entropic stabilization, and is thus thermodynamically inconsistent in the intermediate- and strong-interaction regimes. Our results allow for generalizations to three dimensions, more than two constituents, and conservation laws, which will be addressed in forthcoming publications.

ACKNOWLEDGMENTS

The financial support from the German Research Foundation (DFG) through the Emmy Noether Program Grant No. GO 2762/1-2 (to A.G.) and Project No. ZW 222/3-1 (to D.Z.), and the Max Planck Society (to D.Z. and K.B.), in case of K.B. in the form of an IMPRS fellowship are gratefully acknowledged.

APPENDIX A: MONTE CARLO SIMULATIONS OF THE ISING MODEL

Here we provide details on the Monte Carlo (MC) simulations which we used to determine the ensemble-averaged concentration profile and histograms of instantaneous interface locations displayed in Fig. 1.

1. Lattice setup and initial configuration

We performed MC simulations of the nearest-neighbor interacting ferromagnetic Ising model on the square lattice of size $(N_\sigma^x = 40)\times(N_\sigma^y \in \{80, 90, 100, 110, 120, 130\})$ with single spin-flip dynamics in the bulk and two-spin-exchange dynamics at the boundary columns located at $i = \pm N_\sigma^x/2$. We considered various values of N_σ^y to benchmark our simulations against known theoretical predictions (see Appendix A 5). We imposed periodic boundary conditions in the vertical direction (i.e., along the columns) and free boundary conditions in the horizontal direction (i.e., along the rows), whereby we constrained the total magnetization on the left and right boundaries (see below). Let $N_i^\downarrow$ with $i \in \{-N_\sigma^x/2, \ldots, N_\sigma^x/2\}$ denote the number of down spins in column i. To induce a nonuniform concentration profile, and in anticipation of

known exact results for the bulk concentration values [82], we fixed the number of down spins at the boundaries to be

$$N^{\downarrow}_{\pm N^x_\sigma/2} = \frac{N^y_\sigma}{2}[1 \pm \mathrm{Re}([1-\sinh^{-4}(2J)]^{1/8})], \tag{A1}$$

where J is the coupling strength in units of $k_\mathrm{B}T$. Spins located at the boundaries can exchange *only* within the same column, and therefore the total number of up and down spins at the boundaries is conserved throughout the simulation. Spins in the bulk are initially prepared in a high-coupling configuration (i.e., aligned) with a vertical interface placed at some random horizontal location in the lattice. Starting from a high-coupling configuration has the advantage that the simulations do not get stuck in frozen suboptimal states where multiple interfaces are created [83,84].

2. Acceptance rate

For single spin-flip dynamics let $\{\sigma_j\}'_i$ denote the spin configuration obtained by flipping spin i while keeping the configuration of all other spins fixed, i.e., $\{\sigma_j\}'_i \equiv (-\sigma_i, \{\sigma_{j\neq i}\})$. Moreover, let $p_i(\{\sigma_j\})$ denote the acceptance rate from $\{\sigma_j\}$ to $\{\sigma_j\}'_i$ and $\Delta\mathcal{H}_i(\{\sigma_j\}) \equiv \mathcal{H}(\{\sigma_j\}'_i) - \mathcal{H}(\{\sigma_j\})$ the energy difference (in units of $k_\mathrm{B}T$) associated with the transition. Using the Metropolis algorithm the acceptance rate for the single spin-flip takes the form [85]

$$p_i(\{\sigma_j\}) = \min(1, \mathrm{e}^{-\Delta\mathcal{H}_i(\{\sigma_j\})}). \tag{A2}$$

For two-spin-exchange dynamics let $\{\sigma_j\}'_{ik}$ denote the spin configuration upon interchanging the spins σ_i and σ_k while keeping the configuration of all other spins fixed, i.e., $\{\sigma_j\}'_{ik} \equiv (\sigma_i \leftrightarrow \sigma_k, \{\sigma_{j\neq(i,k)}\})$. We denote with $p_{ik}(\{\sigma_j\})$ the acceptance rate from $\{\sigma_j\}$ to $\{\sigma_j\}'_{ik}$ and $\Delta\mathcal{H}_{ik}(\{\sigma_j\}) \equiv \mathcal{H}(\{\sigma_j\}'_{ik}) - \mathcal{H}(\{\sigma_j\})$ denotes the energy difference associated with the transition. Using the Metropolis algorithm the two-spin-exchange acceptance rate reads as

$$p_{ik}(\{\sigma_j\}) = \min(1, \mathrm{e}^{-\Delta\mathcal{H}_{ik}(\{\sigma_j\})}). \tag{A3}$$

3. Simulation parameters

For each value of the coupling strength J and vertical length $N^y_\sigma \in \{80, 90, 100, 110, 120, 130\}$ we performed $N_\mathrm{MC} = 10^5$ MC simulations, where each individual run contained 5×10^8 MC steps. At each 1.9×10^7th MC step we took a snapshot of the configuration and stored the total energy, resulting in 26 (including the initial configuration) snapshots for each simulation run.

4. Equilibration test: Energy fluctuations per spin

To assess whether the MC simulations reached equilibrium we analyzed the energy fluctuations per spin, and their corresponding ensemble average. In Fig. 6 we display the energy fluctuations per spin for a subset of 10^4 simulations as a function of the MC steps (MCS) for various $J \in \{0.45, 0.7, 0.95, 1.2\}$ and $N^y_\sigma \in \{80, 100, 120, 130\}$. In each plot we observe that immediately after the initial snapshot the energy is fluctuating around an average steady state denoted with the black solid line, providing a first indication that the simulations have reached equilibrium (already at the first stored configuration). Note that in each plot all energies are initially increasing from zero since we subtract the ground-state energy *and* initialize the system in a high-coupling configuration which is identical to the ground state.

5. Benchmark test: Interface width and roughening

To benchmark the performance of our MC simulations we computed the interface width $w^2(N^y_\sigma, J)$ and compared our results with known theoretical results reported in [42,69]. The results from [69] predict $w^2(N^y_\sigma, J) \propto N^y_\sigma/\sinh(\sigma)$ with $\sigma = 2J + \ln\tanh J$. Analogously, the results from [42] predict $w^2(N^y_\sigma, J) = N^y_\sigma/12\sigma - c/2\pi\sigma^2$ with $c \approx 1$. Below we explain in detail how we determined the interface width and how it compares to the theoretical predictions. The resulting outcomes are shown in Fig. 7 and the comparison with the theoretical results are shown in Figs. 7(e) and 7(f).

a. Ensemble-averaged concentration profile and the boundary-shift method

To compare our results with [42,69] we need to apply the so-called boundary-shift method [86] where we shift the interface position of each instantaneous concentration profile to the center of the lattice. As a scientific exercise we also consider the resulting outcomes without applying the boundary-shift method, for which the results are depicted in the top row of Fig. 7. Let $\hat{\varphi}_{i,k}$ be the equilibrated and boundary-shifted (from now on indicated with a hat) concentration of down spins in column i of the kth MC simulation run. The ensemble-average boundary-shifted concentration profile is given by

$$\langle\hat{\varphi}_i\rangle = \frac{1}{N_\mathrm{MC}}\sum_{k=1}^{N_\mathrm{MC}}\hat{\varphi}_{i,k}. \tag{A4}$$

From Eq. (A4) we can approximate the mean interface width using the central difference method as follows:

$$\hat{w}^2(N^y_\sigma, J) = \frac{\sum_{i=-N^x_\sigma/2+1}^{N^x_\sigma/2-1} i^2(\langle\hat{\varphi}_{i+1}\rangle - \langle\hat{\varphi}_{i-1}\rangle)}{\sum_{i=-N^x_\sigma/2+1}^{N^x_\sigma/2-1}\langle\hat{\varphi}_{i+1}\rangle - \langle\hat{\varphi}_{i-1}\rangle} - \left(\frac{\sum_{i=-N^x_\sigma/2+1}^{N^x_\sigma/2-1} i(\langle\hat{\varphi}_{i+1}\rangle - \langle\hat{\varphi}_{i-1}\rangle)}{\sum_{i=-N^x_\sigma/2+1}^{N^x_\sigma/2-1}\langle\hat{\varphi}_{i+1}\rangle - \langle\hat{\varphi}_{i-1}\rangle}\right)^2. \tag{A5}$$

A similar definition holds for the interface width without applying the boundary-shift method, which we denote as $w^2(N^y_\sigma, J)$. In Figs. 7(a)–7(d) we plot $w^2(N^y_\sigma, J)$ and $\hat{w}^2(N^y_\sigma, J)$ with the green dots as a function of N^y_σ. Both results show a clear linear trend with N^y_σ, providing a first validation of the MC simulations. To obtain the variance of $\hat{w}^2(N^y_\sigma, J)$ and $w^2(N^y_\sigma, J)$, which we will use in the next section, we used the jackknife method which is explained below.

b. Interface width and weighted linear regression

To compare our results with those reported in [42,69] we need to extract the interception point $\hat{w}^2(J, 0)$ and slope $d\hat{w}^2(J, N^y_\sigma)/dN^y_\sigma$. Both quantities are obtained with weighted linear regression in combination with the jackknife method. First, we determine $\hat{w}^2(0, J)$ and $d\hat{w}^2(N^y_\sigma, J)/dN^y_\sigma$ while

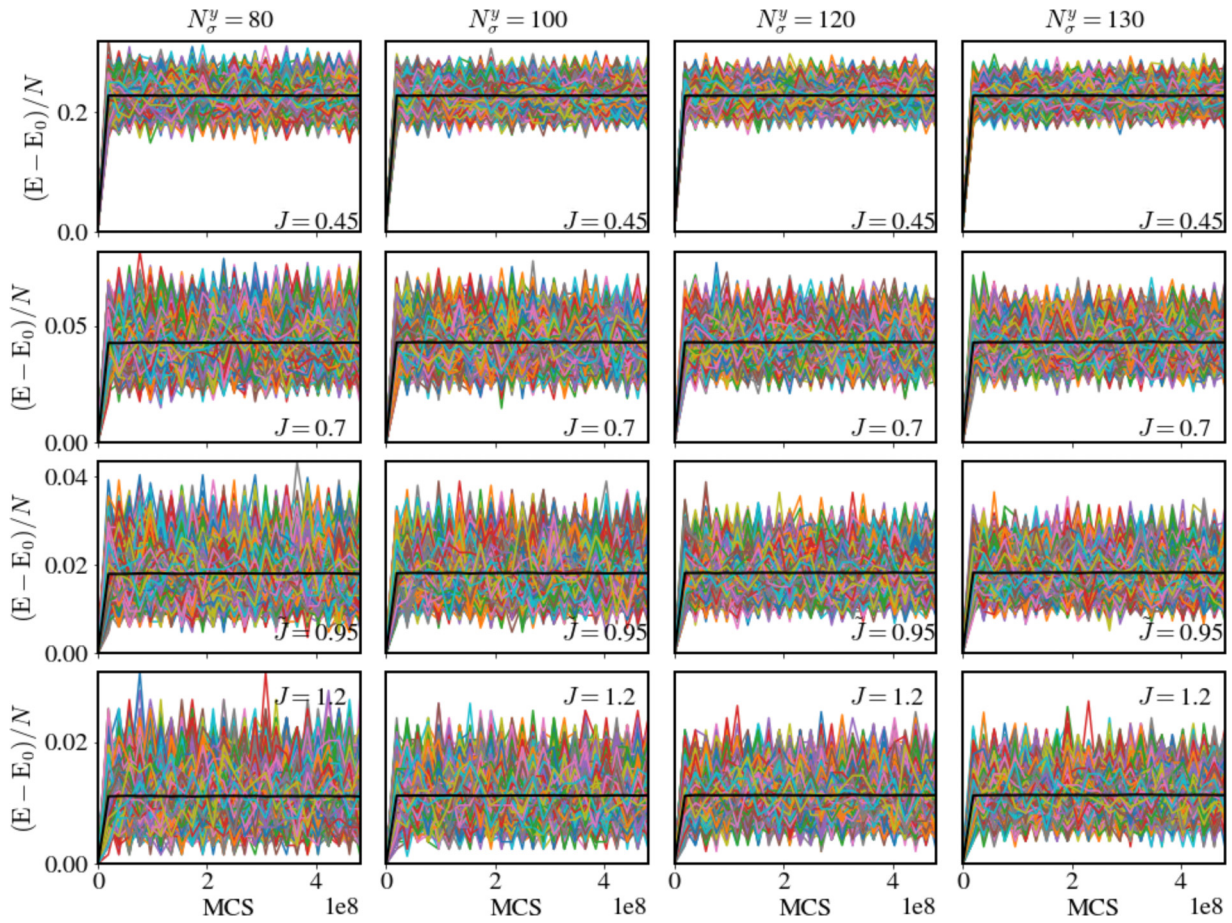

FIG. 6. Equilibration test: energy fluctuations per spin as a function of consecutively stored Monte Carlo (MC) configurations (see text). In each plot we display the energy fluctuations per spin $(E - E_0)/N$ where E_0 is the ground-state energy conditioned on antisymmetric boundary conditions and $N = N_\sigma^x N_\sigma^y$ with $N_\sigma^x = 40$ for a subset of 10^4 MC simulations (colored lines). The black solid line indicates the ensemble-average energy fluctuation per spin. Plots in the same column have equal $N_\sigma^y \in \{80, 100, 120, 130\}$, and plots in the same row have equal $J \in \{0.45, 0.6, 0.95, 1.2\}$.

removing one point from the data pool, which gives

$$\left\{ \hat{w}_j^2(0,J),\ \frac{d\hat{w}_j^2\left(N_\sigma^y,J\right)}{dN_\sigma^y} \right\} = \min_{(\alpha,\beta)} \sum_{\substack{N_\sigma^y=\{80,\ldots,130\} \\ N_\sigma^y \neq 70+10\times j}} \frac{\left[\alpha + \beta N_\sigma^y - \hat{w}^2\left(N_\sigma^y,J\right)\right]^2}{\mathrm{var}\left(\hat{w}^2\left(N_\sigma^y,J\right)\right)}, \quad \text{(A6)}$$

where $j = \{1, \ldots, 6\}$. A similar definition holds for the intersection point and slope without applying the boundary-shift method, which we denote as $w_j^2(0,J)$ and $dw_j^2(N_\sigma^y,J)/dN_\sigma^y$, respectively. Finally, the jackknife ensemble averages and variances are given by

$$\hat{w}^2(0,J) = \frac{1}{6}\sum_{j=1}^{6} \hat{w}_j^2(0,J),$$

$$\mathrm{var}(\hat{w}^2(0,J)) = \frac{5}{6}\sum_{j=1}^{6} \left[\hat{w}_j^2(0,J) - \hat{w}^2(0,J)\right]^2,$$

$$\frac{d\hat{w}^2\left(N_\sigma^y,J\right)}{dN_\sigma^y} = \frac{1}{6}\sum_{j=1}^{6} \frac{d\hat{w}_j^2\left(N_\sigma^y,J\right)}{dN_\sigma^y},$$

$$\mathrm{var}\left(\frac{d\hat{w}^2\left(N_\sigma^y,J\right)}{dN_\sigma^y}\right) = \frac{5}{6}\sum_{j=1}^{6} \left(\frac{d\hat{w}_j^2\left(N_\sigma^y,J\right)}{dN_\sigma^y} - \frac{d\hat{w}^2(N_\sigma^y,J)}{dN_\sigma^y}\right)^2.$$

In Figs. 7(e) and 7(f) we plot $\hat{w}^2(0,J)$ and $d\hat{w}^2(N_\sigma^y,J)/dN_\sigma^y$ together with the standard deviation as a function of J. The theoretical results given by [42,69] are shown with the red and blue lines, respectively. For $J \geqslant 0.6$ we find a very good agreement between MC simulations and theoretical predictions. Notably, for the slope in Fig. 7(f) we find a remarkable agreement with the results of [69]. For $J < 0.6$ we approach the critical coupling $J_{\mathrm{crit}} \approx 0.441$, where the MC results agree less well with theoretical predictions due to finite-size effects. This is expected since the correlation length diverges around the critical coupling.

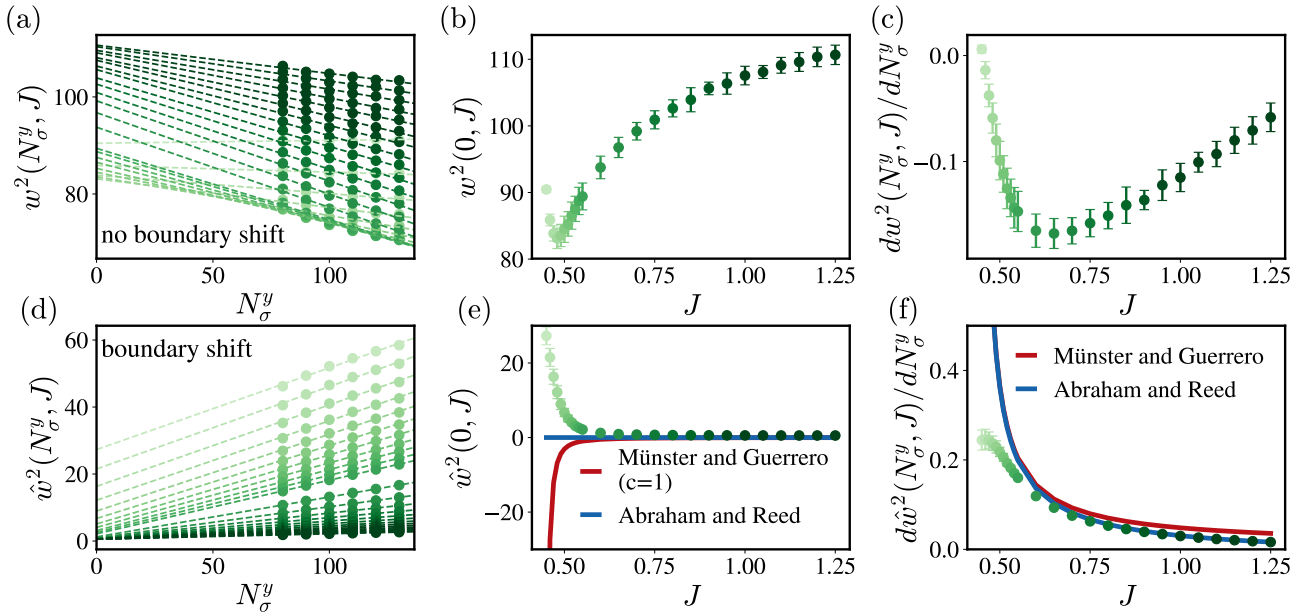

FIG. 7. Benchmark test: results in the top and bottom rows are derived without and with applying the boundary-shift method, respectively. (a)–(d) Scaling of the interface width (a) $w^2(N_\sigma^y, J)$ (no boundary shift) and (d) $\hat{w}^2(N_\sigma^y, J)$ (boundary shift) with respect to the vertical number of spins N_σ^y. Each point is obtained by averaging over 2.5×10^6 equilibrated configurations. Dashed lines are obtained by weighted linear regression. Colors from light green to dark green correspond to increasing coupling strength J. (b)–(e) Intersection point of the interface width at $N_\sigma^y = 0$ as a function of J. The standard deviation of each point is estimated with the jackknife method. In (e) the red and blue lines are the theoretical predictions for the intersection point given in [42,69], respectively. (c)–(f) Slope of the interface width with respect to N_σ^y as a function of J. The standard deviation of each point is estimated with the jackknife method. In (f) the red and blue lines are the theoretical predictions for the slope given in [42,69], respectively.

APPENDIX B: MEAN FIELD APPROXIMATION

Here we derive a Cahn-Hilliard free energy based on the mean field (MF) approximation. Our aim is to evaluate the coarse-grained partition function per spin block $\mathcal{Z}_{ij}$ given by Eq. (17).

1. Approximation of the fraction of defects

On the MF level we introduce the following approximation of the fraction of defects between two spin blocks b_{ij} and b_{mn}:

$$\hat{\zeta}_{\mathrm{MF}}(\varphi_{ij}, \varphi_{mn}) \equiv [\varphi_{ij}(1-\varphi_{mn}) + \varphi_{mn}(1-\varphi_{ij})]/2. \tag{B1}$$

Thus, on the MF level we approximate the number of defects between blocks b_{ij} and b_{mn} by the product of the *spin-down* concentration in box b_{ij} and *spin-up* concentration in box b_{mn}, and vice versa. Making the substitutions

$$\begin{aligned}\zeta_{ij}^{x,y} &\to \hat{\zeta}_{\mathrm{MF}}(\varphi_{ij}, \varphi_{ij}),\\ \xi_{ij}^{x\pm} &\to \hat{\xi}_{\mathrm{MF}}^{x\pm} \equiv \hat{\zeta}_{\mathrm{MF}}(\varphi_{i\pm1 j}, \varphi_{ij}),\\ \xi_{ij}^{y\pm} &\to \hat{\xi}_{\mathrm{MF}}^{y\pm} \equiv \hat{\zeta}_{\mathrm{MF}}(\varphi_{ij\pm1}, \varphi_{ij}),\end{aligned}$$

we see that $\mathcal{H}_{\mathrm{inter}}$ and $\mathcal{H}_{\mathrm{intra}}$ inside the exponent of Eq. (17) become independent of the variables $(\zeta_{ij}^{x,y}, \xi_{ij}^{x,y\pm})$ and only depend on φ_{ij}. Therefore, we can directly use Eq. (18) to perform the four inner sums in Eq. (17). This results in the MF partition function

$$\mathcal{Z}_{ij}^{\mathrm{MF}} = \sum_{\varphi_{ij}} \binom{N_\sigma^b}{\varphi_{ij} N_\sigma^b} \mathrm{e}^{-N_\sigma^b[z_x J_x(\hat{\zeta}_{\mathrm{MF}} + \{\hat{\xi}_{\mathrm{MF}}^{x+} + \hat{\xi}_{\mathrm{MF}}^{x-}\}/2) + (x\leftrightarrow y) - \mathcal{C}]}. \tag{B2}$$

To evaluate the sum over φ_{ij} in Eq. (B2) we employ the maximum term method, and take the maximum term of the continuous summand in the thermodynamic limit [defined in Eq. (9)]. To that end we introduce the MF free-energy density

$$\begin{aligned}\mathrm{f}_{\mathrm{MF}}(\varphi_{i\pm1 j}, \varphi_{ij}, \varphi_{ij\pm1}) &\equiv \lim_{\mathrm{s}}^{\mathbf{N}_\sigma} \left\{ -\left(N_\sigma^b\right)^{-1} \ln\left[\binom{N_\sigma^b}{\varphi_{ij} N_\sigma^b} \mathrm{e}^{-N_\sigma^b[z_x J_x(\hat{\zeta}_{\mathrm{MF}} + \{\hat{\xi}_{\mathrm{MF}}^{x+} + \hat{\xi}_{\mathrm{MF}}^{x-}\}/2) + (x\leftrightarrow y) - \mathcal{C}]} \right] \right\}\\ &= \Xi(\varphi_{ij}) + \Xi(1-\varphi_{ij}) + \left\{ z_x J_x\left(\hat{\zeta}_{\mathrm{MF}} + \left\{\hat{\xi}_{\mathrm{MF}}^{x+} + \hat{\xi}_{\mathrm{MF}}^{x-}\right\}/2\right) + (x\leftrightarrow y)\right\} - \mathcal{C},\end{aligned} \tag{B3}$$

where we used Stirling's approximation $\ln(n!) = \Xi(n) - n + O[\ln(n)]$ with $\Xi(n) \equiv n\ln(n)$ to evaluate the logarithm of the binomial coefficient. Comparing Eq. (B3) with Eq. (26) we notice that the BG free-energy density has considerably

more terms than its MF counterpart due to the functional form of the degeneracy factor. Note that so far we have only taken the thermodynamic limit of the spins. This makes $\varphi_{ij} \in [0, 1]$ a continuous variable, as well as $\hat{\xi}_{\rm MF} \in [0, 1/4]$ and $\hat{\xi}^{x,y\pm}_{\rm MF} \in [0, 1/2]$. Upon considering the thermodynamic limit of the spin blocks, we can employ two different strategies (as proposed in Sec. V G):

(1) First optimize $\mathrm{f}_{\rm MF}(\varphi_{i\pm1j}, \varphi_{ij}, \varphi_{ij\pm1})$ over φ_{ij} and finally apply $\lim_{\rm s}^{\mathbf{N}_b}[\cdot]$.

(2) First apply $\lim_{\rm s}^{\mathbf{N}_b}[\mathrm{f}_{\rm MF}(\varphi_{i\pm1j}, \varphi_{ij}, \varphi_{ij\pm1})]$ and then optimize the resulting free-energy functional.

Below we carry out both, and show that they give equivalent results for the resulting concentration profile. Only the second strategy, however, leads to a Cahn-Hilliard–type free-energy functional.

2. Evaluation of the partition function: Strategy 1

Using the maximum term method we need to find the location φ_{ij} which renders $\mathrm{f}_{\rm MF}(\varphi_{i\pm1j}, \varphi_{ij}, \varphi_{ij\pm1})$ minimal, yielding the equation

$$\partial_{\varphi_{ij}}\left[\mathrm{f}_{\rm MF}(\varphi_{i\pm1j}, \varphi_{ij}, \varphi_{ij\pm1}) + \sum_{k=\pm1}[\mathrm{f}_{\rm MF}(\varphi_{i+k\pm1j}, \varphi_{i+kj}, \varphi_{i+kj\pm1}) + \mathrm{f}_{\rm MF}(\varphi_{i\pm1j+k}, \varphi_{ij+k}, \varphi_{ij+k\pm1}]\right] \stackrel{!}{=} 0, \tag{B4}$$

where $\partial_{\varphi_{ij}} \equiv \partial/\partial\varphi_{ij}$. Note that additionally to $\mathrm{f}_{\rm MF}(\varphi_{i\pm1j}, \varphi_{ij}, \varphi_{ij\pm1})$, four extra terms enter Eq. (B4) which also contain an explicit dependence on φ_{ij}. The solution to Eq. (B4) can be cast into the following set of difference equations:

$$z_xJ_x(\varphi_{i+1j} - 2\varphi_{ij} + \varphi_{i-1j}) + z_yJ_y(\varphi_{ij+1} - 2\varphi_{ij} + \varphi_{ij-1}) = 2(z_xJ_x + z_yJ_y)(1 - 2\varphi_{ij}) - \ln(1/\varphi_{ij} - 1), \tag{B5}$$

for $(i, j) \in (\{1, \ldots, N_b^x\}, \{1, \ldots, N_b^y\})$. Now we can carry out the scaling limit of the spin blocks, for which we introduce the following notation:

$$\begin{aligned}
&\lim_{\rm s}^{\mathbf{N}_b}[\varphi_{ij} = \varphi(il_x, jl_y)] \equiv \varphi(x, y), \quad \forall\,(x, y) \in A\\
&\lim_{\rm s}^{\mathbf{N}_b}[\varphi_{i\pm1j} = \varphi(il_x \pm l_x, jl_y)] \equiv \lim_{l_x\to0}\varphi(x \pm l_x, y), \quad \forall\,(x, y) \in A\\
&\lim_{\rm s}^{\mathbf{N}_b}[\varphi_{ij\pm1} = \varphi(il_x, jl_y \pm l_y)] \equiv \lim_{l_y\to0}\varphi(x, y \pm l_y), \quad \forall\,(x, y) \in A
\end{aligned} \tag{B6}$$

where $A = [-L_x/2, L_x/2]\times[-L_y/2, L_y/2]$. Applying $\lim_{\rm s}^{\mathbf{N}_b}[\cdot]$ to both sides of Eq. (B5) we obtain the following partial differential equation:

$$z_xJ_xl_x^2\partial_x^2\varphi(x, y) + z_yJ_yl_y^2\partial_y^2\varphi(x, y) = 2(z_xJ_x + z_yJ_y)[1 - 2\varphi(x, y)] - \ln[1/\varphi(x, y) - 1], \ \forall\,(x, y) \in A \tag{B7}$$

where we used

$$\begin{aligned}
&\lim_{l_x\to0}[\varphi(x + l_x, y) - 2\varphi(x, y) + \varphi(x - l_x, y)] = l_x^2\partial^2\varphi(x, y)/\partial x^2,\\
&\lim_{l_y\to0}[\varphi(x, y + l_y) - 2\varphi(x, y) + \varphi(x, y - l_y)] = l_y^2\partial^2\varphi(x, y)/\partial y^2.
\end{aligned}$$

Upon specifying the boundary conditions the solution to Eq. (B7) gives the equilibrium concentration profile and maximizes the MF partition function in the thermodynamic limit.

3. Evaluation of the partition function: Strategy 2

To apply the thermodynamic limit of the spin blocks to Eq. (B3) we first add and subtract $z_xJ_x\hat{\xi}_{\rm MF}$ inside the third term. Next, we use Eq. (B6) and obtain the following intermediate results:

$$\begin{aligned}
&\lim_{l_x\to0}[\hat{\xi}_{\rm MF}(\varphi(x+l_x, y), \varphi(x, y)) - 2\hat{\xi}_{\rm MF}(\varphi(x, y), \varphi(x, y)) + \hat{\xi}_{\rm MF}(\varphi(x-l_x, y), \varphi(x, y))] = l_x^2[1-\varphi(x, y)]\partial_x^2\varphi(x, y),\\
&\lim_{l_y\to0}[\hat{\xi}_{\rm MF}(\varphi(x, y+l_y), \varphi(x, y)) - 2\hat{\xi}_{\rm MF}(\varphi(x, y), \varphi(x, y)) + \hat{\xi}_{\rm MF}(\varphi(x, y-l_y), \varphi(x, y))] = l_y^2[1-\varphi(x, y)]\partial_y^2\varphi(x, y).
\end{aligned} \tag{B8}$$

Inserting the outcome of Eq. (B8) into Eq. (B3) we obtain the following result in the thermodynamic limit:

$$\lim_{\rm s}^{\mathbf{N}_b}[\mathrm{f}_{\rm MF}(\varphi_{i\pm1j}, \varphi_{ij}, \varphi_{ij\pm1})] = \mathrm{f}_{\rm MF}(\varphi(x, y)) + [1 - \varphi(x, y)]\big[z_xJ_xl_x^2\partial_x^2\varphi(x, y) + z_yJ_yl_y^2\partial_y^2\varphi(x, y)\big]/2, \tag{B9}$$

where the MF local free-energy density is given by

$$\mathrm{f}_{\rm MF}(\varphi) \equiv \Xi(\varphi) + \Xi(1 - \varphi) + 2(z_yJ_y + z_xJ_x)[\varphi(1 - \varphi) - 1/4]. \tag{B10}$$

Finally, we construct the MF free-energy functional which is given by (recall that $N_b = N_b^x\times N_b^y$)

$$\begin{aligned}
F_{\rm MF}[\varphi(x, y)] &\equiv \lim_{\rm s}^{\mathbf{N}_b}\left[(N_b)^{-1}\sum_{i=1}^{N_b^x}\sum_{j=1}^{N_b^y}\mathrm{f}_{\rm MF}(\varphi_{i\pm1j}, \varphi_{ij}, \varphi_{ij\pm1})\right]\\
&= \frac{1}{l_xl_y}\int_{(x,y)\in A}\big\{\mathrm{f}_{\rm MF}(\varphi(x, y)) + [1 - \varphi(x, y)]\big[z_xJ_xl_x^2\partial_x^2\varphi(x, y) + z_yJ_yl_y^2\partial_y^2\varphi(x, y)\big]/2\big\}dx\,dy\\
&\stackrel{\rm P.I.}{=} \frac{1}{l_xl_y}\int_{(x,y)\in A}\big[\mathrm{f}_{\rm MF}(\varphi(x, y)) + z_xJ_xl_x^2(\partial_x\varphi(x, y))^2/2 + z_yJ_yl_y^2(\partial_y\varphi(x, y))^2/2\big]dx\,dy,
\end{aligned} \tag{B11}$$

where in the last line we carried out a partial integration (P.I.) and used zero-flux boundary conditions $\partial_y\varphi(x,\pm L_y/2) = \partial_x\varphi(\pm L_x/2, y) = 0$ (which we will assume in later sections). The profile $\varphi(x, y)$ which constitutes a stationary point of Eq. (B11), i.e., $\delta F_{\mathrm{MF}}[\varphi(x, y)]/\delta\varphi(x, y) = 0$, is obtained by solving the corresponding Euler-Lagrange equation

$$z_x J_x l_x^2 \partial_x^2\varphi(x, y) + z_y J_y l_y^2 \partial_y^2\varphi(x, y) = \partial_{\varphi(x,y)} \mathrm{f}_{\mathrm{MF}}(\varphi(x, y)), \quad \forall\ (x, y) \in A. \tag{B12}$$

Plugging Eq. (B10) into Eq. (B12) finally results in Eq. (B7).

APPENDIX C: BETHE-GUGGENHEIM APPROXIMATION

1. Introduction

Our starting point within the BG approximation is the free-energy density given by Eq. (26). As with the MF calculation we will consider two different strategies for evaluating the partition function. The second strategy has already been discussed in Sec. V G, and here we provide some further details about the calculation.

2. Evaluation of the partition function: Strategy 1

The local minima of Eq. (26) with respect to φ_{ij} are given by the following equation:

$$\partial_{\varphi_{ij}}\left[\mathrm{f}(\varphi_{i\pm1j}, \varphi_{ij}, \varphi_{ij\pm1}) + \sum_{k=\pm1}[\mathrm{f}(\varphi_{i+k\pm1j}, \varphi_{i+kj}, \varphi_{i+kj\pm1}) + \mathrm{f}(\varphi_{i\pm1j+k}, \varphi_{ij+k}, \varphi_{ij+k\pm1})]\right] \stackrel{!}{=} 0. \tag{C1}$$

Upon taking the partial derivative of the BG local free-energy density with respect to φ_{ij}, we can use the following:

$$\partial_{\hat\zeta_\dagger^{x,y}}\mathrm{f}(\varphi_{i\pm1j}, \varphi_{ij}, \varphi_{ij\pm1}) = \partial_{\hat\xi_\dagger^{x,y\pm}}\mathrm{f}(\varphi_{i\pm1j}, \varphi_{ij}, \varphi_{ij\pm1}) = 0, \tag{C2}$$

since both $\hat\zeta_\dagger^{x,y}$ and $\hat\xi_\dagger^{x,y\pm}$ are obtained by minimization of the BG free-energy density. This renders the evaluation of Eq. (C1) a relatively easy task and results in the following recurrent set of difference equations:

$$\begin{aligned}
&\frac{z_x}{8}\sum_{\pm}\left[\ln\left(\frac{1-\varphi_{ij}-\hat\xi_\dagger^{x\pm}(\varphi_{i\pm1j}, \varphi_{ij})}{\varphi_{ij}-\varphi_{i\pm1j}+\hat\xi_\dagger^{x\pm}(\varphi_{i\pm1j}, \varphi_{ij})}\right) - \ln\left(\frac{\varphi_{ij}-\hat\xi_\dagger^{x\pm}(\varphi_{ij}, \varphi_{i\pm1j})}{\varphi_{i\pm1j}-\varphi_{ij}+\hat\xi_\dagger^{x\pm}(\varphi_{ij}, \varphi_{i\pm1j})}\right)\right] \\
&+\frac{z_y}{8}\sum_{\pm}\left[\ln\left(\frac{1-\varphi_{ij}-\hat\xi_\dagger^{y\pm}(\varphi_{ij\pm1}, \varphi_{ij})}{\varphi_{ij}-\varphi_{ij\pm1}+\hat\xi_\dagger^{y\pm}(\varphi_{ij\pm1}, \varphi_{ij})}\right) - \ln\left(\frac{\varphi_{ij}-\hat\xi_\dagger^{y\pm}(\varphi_{ij}, \varphi_{ij\pm1})}{\varphi_{ij\pm1}-\varphi_{ij}+\hat\xi_\dagger^{y\pm}(\varphi_{ij}, \varphi_{ij\pm1})}\right)\right] \\
&= \frac{z_x}{4}\ln\left(\frac{\varphi_{ij}-\hat\zeta_\dagger^{x}(\varphi_{ij}, \varphi_{ij})}{1-\varphi_{ij}-\hat\zeta_\dagger^{x}(\varphi_{ij}, \varphi_{ij})}\right)+(x\leftrightarrow y)+(1-z)\ln\left(\frac{\varphi_{ij}}{1-\varphi_{ij}}\right), \quad \forall\ (i, j) \in \left(\{1, \ldots, N_b^x\}, \{1, \ldots, N_b^y\}\right).
\end{aligned} \tag{C3}$$

For a one-dimensional concentration profile (i.e., $\varphi_{ij} \to \varphi_i$) a similar equation has been derived in [52] [see Eqs. (31)–(33) therein] where the solution is obtained (only) around the critical point. Here we proceed with applying the thermodynamic limit of the spin blocks to Eq. (C3) using Eq. (B6). To obtain the thermodynamic limit we calculate the following terms:

$$\begin{aligned}
&\lim_{l_x\to0}\left[\left(\sum_{\pm}\ln[1-\varphi(x, y)-\hat\xi_\dagger^{x\pm}(\varphi(x\pm l_x, y), \varphi(x, y))]-2\ \ln[1-\varphi(x, y)-\hat\zeta_\dagger^{x}(\varphi(x, y), \varphi(x, y))]\right)\Big/ l_x^2\right] \\
&= \left(\frac{\hat\xi_\dagger^{x(1,0)}}{\varphi(x, y)+\hat\zeta_\dagger^{x}-1}\right)\partial_x^2\varphi(x, y) - \left(\frac{(\hat\xi_\dagger^{x(1,0)})^2}{(\varphi(x, y)+\hat\zeta_\dagger^{x}-1)^2} - \frac{\hat\xi_\dagger^{x(2,0)}}{\varphi(x, y)+\hat\zeta_\dagger^{x}-1}\right)(\partial_x\varphi(x, y))^2,
\end{aligned} \tag{C4}$$

$$\begin{aligned}
&\lim_{l_x\to0}\left[\left(2\ \ln[\varphi(x, y) - \hat\zeta_\dagger^{x}(\varphi(x, y), \varphi(x, y))] - \sum_{\pm}\ln[\varphi(x, y) - \hat\xi_\dagger^{x\pm}(\varphi(x, y), \varphi(x\pm l_x, y))]\right)\Big/ l_x^2\right] \\
&= \left(\frac{\hat\xi_\dagger^{x(0,1)}}{\varphi(x, y) - \hat\zeta_\dagger^{x}}\right)\partial_x^2\varphi(x, y) + \left(\frac{(\hat\xi_\dagger^{x(0,1)})^2}{(\varphi(x, y) - \hat\zeta_\dagger^{x})^2} + \frac{\hat\xi_\dagger^{x(0,2)}}{\varphi(x, y) - \hat\zeta_\dagger^{x}}\right)(\partial_x\varphi(x, y))^2,
\end{aligned} \tag{C5}$$

$$\begin{aligned}
&\lim_{l_x\to0}\left[\left(\sum_{\pm}\ln[\varphi(x\pm l_x, y) - \varphi(x, y) + \hat\xi_\dagger^{x\pm}(\varphi(x, y), \varphi(x\pm l_x, y))] - 2\ \ln[\hat\zeta_\dagger^{x}(\varphi(x, y), \varphi(x, y))]\right)\Big/ l_x^2\right] \\
&= \left(\frac{\hat\xi_\dagger^{x(0,1)}+1}{\hat\zeta_\dagger^{x}}\right)\partial_x^2\varphi(x, y) - \left(\frac{(\hat\xi_\dagger^{x(0,1)}+1)^2}{(\hat\zeta_\dagger^{x})^2} - \frac{\hat\xi_\dagger^{x(0,2)}}{\hat\zeta_\dagger^{x}}\right)(\partial_x\varphi(x, y))^2,
\end{aligned} \tag{C6}$$

$$\lim_{l_x\to 0}\left[\left(2\,\ln[\hat{\zeta}^x_\dagger(\varphi(x,y),\varphi(x,y))]-\sum_{\pm}\ln[\varphi(x,y)-\varphi(x\pm l_x,y)+\hat{\xi}^{x\pm}_\dagger(\varphi(x\pm l_x,y),\varphi(x,y))]\right)\Big/ l_x^2\right]$$
$$=\left(\frac{1-\hat{\xi}^{x(1,0)}_\dagger}{\hat{\zeta}^x_\dagger}\right)\partial_x^2\varphi(x,y)+\left(\frac{(\hat{\xi}^{x(1,0)}_\dagger-1)^2}{(\hat{\zeta}^x_\dagger)^2}-\frac{\hat{\xi}^{x(2,0)}_\dagger}{\hat{\zeta}^x_\dagger}\right)(\partial_x\varphi(x,y))^2, \tag{C7}$$

where $\hat{\xi}^{x(m,n)}_\dagger\equiv\partial_a^m\partial_b^n\hat{\xi}^x_\dagger(a,b)|_{(\varphi(x,y),\varphi(x,y))}$ and we have used that $\hat{\xi}^{x\pm}_\dagger(a,a)=\hat{\zeta}^x_\dagger(a,a)$. Upon interchanging x with y the results of Eqs. (C4)–(C7) also apply to the y direction. Note that the second term on the left-hand side in Eq. (C4) and the first term on the left-hand side in Eq. (C5) are added ad hoc, and therefore also need to be added to the right-hand side of Eq. (C3). The second and first term on the left-hand side in Eqs. (C6) and (C7) directly cancel, and therefore do not need to be added to the right-hand side. Summing up all the contributions we obtain the following expression:

$$\frac{z_x}{8}[(\text{C4})+(\text{C5})+(\text{C6})+(\text{C7})]=\kappa_x(\varphi(x,y))\partial_x^2\varphi(x,y)+\frac{\kappa_x'(\varphi(x,y))(\partial_x\varphi(x,y))^2}{2}, \tag{C8}$$

where the gradient energy coefficient κ_x is given by Eq. (29) and $\kappa_x'(\varphi)=\partial_\varphi\kappa_x(\varphi)$. For a one-dimensional concentration profile (only) this result has also been derived in [51] [see Eq. (2.12b) therein] but so far it has not been derived for a two-dimensional system. Plugging the result back into the left-hand side of Eq. (C3) we obtain the following partial differential equation (PDE):

$$l_x^2\left[\kappa_x\partial_x^2\varphi(x,y)+\kappa_x'(\partial_x\varphi(x,y))^2/2\right]+(x\leftrightarrow y)=\frac{z_x}{2}\ln\left(\frac{\varphi(x,y)-\hat{\zeta}^x_\dagger}{1-\varphi(x,y)-\hat{\zeta}^x_\dagger}\right)+(x\leftrightarrow y)+(1-z)\ln\left(\frac{\varphi(x,y)}{1-\varphi(x,y)}\right), \tag{C9}$$

which applies in the domain $(x,y)\in A$ with $A=[-L_x/2,L_x/2]\times[-L_y/2,L_y/2]$. Recall that $(x\leftrightarrow y)$ denotes a repetition of the preceding term with x substituted by y, and $\hat{\zeta}^{x,y}_\dagger$ is given in Eq. (25). Equation (C9) is the BG equivalent of the MF PDE given by Eq. (B7).

3. Evaluation of the partition function: Strategy 2

Applying the thermodynamic limit to Eq. (26) in the x direction we need to keep track of the following terms:

$$\lim_{l_x\to 0}\left[\left(\sum_{\pm}\hat{\xi}^{x\pm}_\dagger(\varphi(x\pm l_x,y),\varphi(x,y))-2\hat{\zeta}^x_\dagger(\varphi(x,y),\varphi(x,y))\right)\Big/ l_x^2\right]\overset{\text{P.I.}}{=}-(\partial_x\varphi(x,y))^2\hat{\xi}^{x(1,1)}_\dagger, \tag{C10}$$

$$\lim_{l_x\to 0}\left[\left(\sum_{\pm}\Xi(\varphi(x\pm l_x,y))-2\Xi(\varphi(x,y))\right)\Big/ l_x^2\right]=(\partial_x\varphi(x,y))^2/\varphi(x,y)+\partial_x^2\varphi(x,y)[\ln(\varphi(x,y))+1]\overset{\text{P.I.}}{=}0, \tag{C11}$$

$$\lim_{l_x\to 0}\left[\left(\sum_{\pm}\Xi[1-\varphi(x\pm l_x,y)]-2\Xi[1-\varphi(x,y)]\right)\Big/ l_x^2\right]=(\partial_x\varphi(x,y))^2/[1-\varphi(x,y))]-\partial_x^2\varphi(x,y)\{\ln[1-\varphi(x,y)]+1\}\overset{\text{P.I.}}{=}0, \tag{C12}$$

$$\lim_{l_x\to 0}\left[\left(\sum_{\pm}\Xi[\hat{\xi}^{x\pm}_\dagger(\varphi(x\pm l_x,y),\varphi(x,y))]-2\Xi[\hat{\zeta}^x_\dagger(\varphi(x,y),\varphi(x,y))]\right)\Big/ l_x^2\right]$$
$$\overset{\text{P.I.}}{=}-(\partial_x\varphi(x,y))^2\frac{\hat{\xi}^{x(1,0)}_\dagger\hat{\xi}^{x(0,1)}_\dagger}{\hat{\zeta}^x_\dagger}-(\partial_x\varphi(x,y))^2\hat{\xi}^{x(1,1)}_\dagger[\ln(\hat{\zeta}^x_\dagger)+1], \tag{C13}$$

$$\lim_{l_x\to 0}\left[\left(\sum_{\pm}\Xi[\varphi(x\pm l_x,y)-\hat{\xi}^{x\pm}_\dagger(\varphi(x\pm l_x,y),\varphi(x,y))]-2\Xi[\varphi(x,y)-\hat{\zeta}^x_\dagger(\varphi(x,y),\varphi(x,y))]\right)\Big/ l_x^2\right]$$
$$\overset{\text{P.I.}}{=}-(\partial_x\varphi(x,y))^2\frac{(\hat{\xi}^{x(1,0)}_\dagger-1)\hat{\xi}^{x(0,1)}_\dagger}{\varphi(x,y)-\hat{\zeta}^x_\dagger}+(\partial_x\varphi(x,y))^2\hat{\xi}^{x(1,1)}_\dagger\{\ln[\varphi(x,y)-\hat{\zeta}^x_\dagger]+1\}, \tag{C14}$$

$$\lim_{l_x\to 0}\left[\left(\sum_{\pm}\Xi[1-\varphi(x,y)-\hat{\xi}^{x\pm}_\dagger(\varphi(x\pm l_x,y),\varphi(x,y))]-2\Xi[1-\varphi(x,y)-\hat{\zeta}^x_\dagger(\varphi(x,y),\varphi(x,y))]\right)\Big/ l_x^2\right]$$
$$\overset{\text{P.I.}}{=}-(\partial_x\varphi(x,y))^2\frac{\hat{\xi}^{x(1,0)}_\dagger[\hat{\xi}^{x(0,1)}_\dagger+1]}{1-\varphi(x,y)-\hat{\zeta}^x_\dagger}+(\partial_x\varphi(x,y))^2\hat{\xi}^{x(1,1)}_\dagger\{\ln[1-\varphi(x,y)-\hat{\zeta}^x_\dagger]+1\}, \tag{C15}$$

$$\lim_{l_x\to 0}\left[\left(\sum_{\pm}\Xi[\varphi(x,y)-\varphi(x\pm l_x,y)+\hat{\xi}^{x\pm}_\dagger(\varphi(x\pm l_x,y),\varphi(x,y))]-2\Xi[\hat{\zeta}^x_\dagger(\varphi(x,y),\varphi(x,y))]\right)\Big/ l_x^2\right]$$
$$\overset{\text{P.I.}}{=}-(\partial_x\varphi(x,y))^2\frac{(\hat{\xi}^{x(1,0)}_\dagger-1)(\hat{\xi}^{x(0,1)}_\dagger+1)}{\hat{\zeta}^x_\dagger}-(\partial_x\varphi(x,y))^2\hat{\xi}^{x(1,1)}_\dagger[\ln(\hat{\zeta}^x_\dagger)+1], \tag{C16}$$

where we have immediately carried out a partial integration, since each term will arise inside an integral, and used zero-flux boundary conditions $\partial_x\varphi(\pm L_x/2, y) = 0$ to express everything in terms of $(\partial_x\varphi(x, y))^2$. Next, we add up the second terms on the right-hand side in Eqs. (C13)–(C16) and find that they exactly cancel with Eq. (C10) upon plugging them back into Eq. (26). Adding up the first terms in Eqs. (C13)–(C17) and multiplying by $z_x/8$ gives the following result:

$$\frac{1}{2}\kappa_x(\varphi(x, y))(\partial_x\varphi(x, y))^2. \tag{C17}$$

Upon interchanging x with y the same results apply to the y direction. Putting the results back into Eq. (26) and adding or subtracting those terms which have been added by hand in Eqs. (C10)–(C16) we finally obtain the BG free-energy density in the scaling limit of the blocks

$$\begin{aligned}\lim_{\mathrm{s}}^{\mathbf{N}_b}&[\mathrm{f}(\varphi_{i\pm1j}, \varphi_{ij}, \varphi_{ij\pm1})]\\ &= \mathrm{f}(\varphi(x, y)) + \frac{l_x^2}{2}\kappa_x(\varphi(x, y))(\partial_x\varphi(x, y))^2\\ &\quad + \frac{l_y^2}{2}\kappa_y(\varphi(x, y))(\partial_y\varphi(x, y))^2,\end{aligned} \tag{C18}$$

where $\kappa_{x,y}(\varphi)$ is defined in Eq. (29), and the BG local free-energy density $\mathrm{f}(\varphi)$ is given by Eq. (28). Finally, the BG free-energy density functional is given by Eq. (27). The profile $\varphi(x, y)$ which constitutes a stationary point of Eq. (27), i.e., $\delta F[\varphi(x, y)]/\delta\varphi(x, y) = 0$, is obtained by solving the corresponding Euler-Lagrange equation

$$l_x^2\left[\kappa_x\partial_x^2\varphi(x, y) + \frac{\kappa_x'(\partial_x\varphi(x, y))^2}{2}\right] + (x \leftrightarrow y) = \frac{\partial \mathrm{f}(\varphi(x, y))}{\partial\varphi(x, y)}, \tag{C19}$$

which is equivalent to Eq. (C9).

APPENDIX D: EQUILIBRIUM CONCENTRATION PROFILE

Here we consider a concentration profile which only varies in the x direction, i.e., $\varphi(\mathbf{x}) = \varphi(x),\ \forall\, x \in [-L_x/2, L_x/2]$. The equilibrium profile $\varphi(x)$ is an extremum of Eqs. (B11) and (27) for the MF and BG approximation, respectively. Here we will derive analytical expressions for the interface steepness, interface width (according to the Cahn-Hilliard definition), and prove the broadening of the BG equilibrium profile.

1. Results within mean field theory

For a one-dimensional concentration profile Eq. (B12) reduces to a second-order autonomous ordinary differential equation (ODE). Therefore, we can directly obtain the interface steepness $\varphi'_{\mathrm{MF}}(x)$, which reads as

$$\varphi'_{\mathrm{MF}}(x) = \pm\sqrt{2[\mathrm{f}_{\mathrm{MF}}(\varphi_{\mathrm{MF}}(x)] - \mathrm{f}_{\mathrm{MF}}(\varphi_{\mathrm{MF,min}})/z_xJ_x}, \tag{D1}$$

where we have set the integration constant to $\mathcal{C}_1 = -\mathrm{f}_{\mathrm{MF}}(\varphi_{\mathrm{MF,min}})$ with $\varphi_{\mathrm{MF,min}} \equiv \arg\inf_{0\leqslant\varphi\leqslant1/2}\ \mathrm{f}_{\mathrm{MF}}(\varphi)$ such that the term inside the square root on the right-hand side is always positive and $\lim_{x\to\pm\infty}\varphi'_{\mathrm{MF}}(x) = 0$. The location of the global minimum of the uniform MF free-energy density can be written as $\varphi_{\mathrm{MF,min}} \equiv (1 - |s|)/2$, where $s \in [-1, 1]$ is given by the nonzero solutions to the so-called transcendental mean field equation [77]

$$s = \tanh\left([z_xJ_x + z_yJ_y]s\right). \tag{D2}$$

Below the critical coupling for $z_xJ_x + z_yJ_y \leqslant 1$ the only solution to Eq. (D2) is given by $s = 0$, resulting in $\varphi_{\mathrm{MF,min}} = 1/2$. Above the critical coupling for $z_xJ_x + z_yJ_y > 1$ there exist two nonzero solutions resulting in $\varphi_{\mathrm{MF,min}} < 1/2$. Now let us focus on the isotropic case with a vanishing external field, i.e., $J_x = J_y = J$, and consider the interface steepness at $x = 0$. Based on the imposed boundary conditions we know that $\varphi_{\mathrm{MF}}(0) = 1/2$, and therefore the interface steepness at $x = 0$ reads as

$$\varphi'_{\mathrm{MF}}(0) = \pm\sqrt{2[\mathrm{f}_{\mathrm{MF}}(1/2) - \mathrm{f}_{\mathrm{MF}}(\varphi_{\mathrm{MF,min}})]/z_xJ}. \tag{D3}$$

For a square lattice with $\{z_x, z_y\} = \{2, 2\}$ Eq. (D3) is shown in Fig. 4(b) with the red solid line. To obtain the interface width as defined by Cahn and Hilliard [see Eq. (2.25) in [1]] we simply need take a line tangential to the slope of the concentration profile at $x = 0$ and determine the crossing points of this line with the bulk concentration values as depicted in Fig. 8(a). This leads to the expression

$$l_{\mathrm{MF,CH}} = (1 - 2\varphi_{\mathrm{MF,min}})/\varphi'_{\mathrm{MF}}(0), \tag{D4}$$

where we insert Eq. (D3) for $\varphi'_{\mathrm{MF}}(0)$ with the positive sign. We see that for $zJ \leqslant 1$ we have $l_{\mathrm{MF,CH}} \to \infty$. Now let us consider an infinite coupling strength. In this limit the nonzero solutions to Eq. (D2) are trivially given by $s = \pm1,\ \forall\, z > 0$, and therefore we obtain

$$\begin{aligned}\lim_{J\to\infty}\varphi'_{\mathrm{MF}}(0) &= \lim_{J\to\infty}\pm\sqrt{2[\mathrm{f}_{\mathrm{MF}}(1/2) - \mathrm{f}_{\mathrm{MF}}(0)]/z_xJ}\\ &= \lim_{J\to\infty}\pm\sqrt{2[zJ/2 - \ln(2)]/z_xJ} = \pm\sqrt{z/z_x}.\end{aligned} \tag{D5}$$

Hence, in the infinite coupling limit the interface steepness converges to a maximum finite nonzero value. This value for the MF interface steepness is also reported in Fig. 4(b). Furthermore, the interface width decreases and converges to the value

$$\lim_{J\to\infty} l_{\mathrm{MF,CH}} = \lim_{J\to\infty}(1 - 2\varphi_{\mathrm{MF,min}})/\varphi'_{\mathrm{MF}}(0) = \sqrt{z_x/z}. \tag{D6}$$

2. Results within Bethe-Guggenheim theory

Similar to the MF analysis Eq. (C19) reduces to a second-order autonomous ODE for a one-dimensional concentration profile. To obtain the interface steepness we first rewrite the left-hand side of Eq. (C19) as

$$\kappa_x\varphi''(x) + \kappa_x'(\varphi'(x))^2/2 = \frac{1}{2\varphi'(x)}\frac{d}{dx}[\kappa_x(\varphi'(x))^2]. \tag{D7}$$

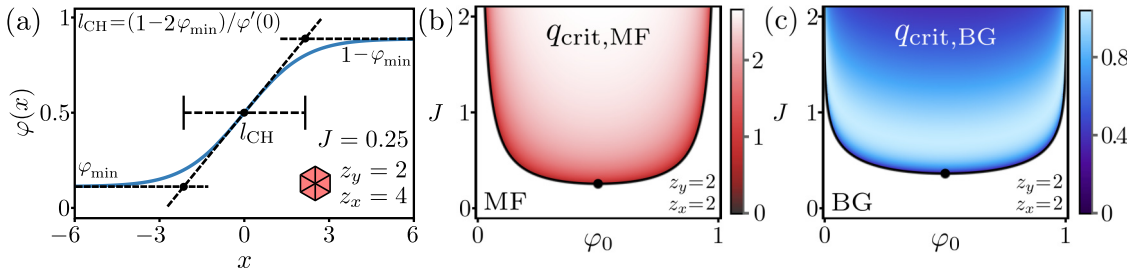

FIG. 8. (a) Representation of the Cahn-Hilliard interface width l_{CH} given by Eq. (D4). Here we used the concentration profile for a hexagonal ($z = 6$) lattice obtained with the BG approximation. (b) Critical wave vector obtained with the MF approximation (E5) for a square lattice. The black line represents the MF spinodal and the black dot the MF critical point $J_{crit,MF} = 1/4$. (c) Critical wave vector obtained with the BG approximation (36) for a square lattice. The black line represents the BG spinodal and the black dot the BG critical point $J_{crit,BG} = \ln(2)/2$.

Taking the term $1/\varphi'(x)$ to the right-hand side of Eq. (C19) and using the fact that $\varphi'(x)[\partial \mathrm{f}(\varphi(x))/\partial\varphi(x)] = d\mathrm{f}(\varphi(x))/dx$, we can integrate both sides over x, resulting in the first-order autonomous ODE

$$\tfrac{1}{2}\kappa_x(\varphi'(x))^2 = \mathrm{f}(\varphi(x)) + \mathcal{C}_1, \tag{D8}$$

where $\mathcal{C}_1$ is an integration constant. From Eq. (D8) we can directly read out the interface steepness

$$\varphi'(x) = \pm\sqrt{2[\mathrm{f}(\varphi(x)) - \mathrm{f}(\varphi_{min})]/\kappa_x(\varphi(x))}, \tag{D9}$$

where we have set the integration constant $\mathcal{C}_1 = -\mathrm{f}(\varphi_{min})$ with $\varphi_{min} \equiv \inf_{0\leqslant\varphi\leqslant 1/2} \mathrm{f}(\varphi)$. The integration constant is chosen such that the term inside the square root on the right-hand side is always positive and to impose a vanishing derivative at the boundaries. Now let us focus specifically on the isotropic case with a vanishing external field, i.e., $J_x = J_y = J$. The location of the global minimum φ_{min} of the local BG free-energy density can be written as $\varphi_{min} = \chi_\varphi/(1+\chi_\varphi)$, where $\chi_\varphi \in [0,\infty)$ is given by the nontrivial solutions (i.e., $\chi_\varphi \neq 1$) to the transcendental equation (see also [77])

$$\chi_\varphi - \mathrm{e}^{2J}\left[\chi_\varphi^{(z-1)/z} - \chi_\varphi^{1/z}\right] - 1 = 0. \tag{D10}$$

Below and at the critical coupling $J \leqslant J_{BG,crit}$, Eq. (D10) has one trivial solution $\chi_\varphi = 1$, resulting in $\varphi_{min} = 1/2$. Above the critical coupling there exist two nontrivial solutions, resulting in $\varphi_{min} < 1/2$. Equation (D10) cannot be solved analytically for general z but is explicitly solvable for a triangular, square, and hexagonal lattice, which gives

$$\begin{aligned}
\varphi_{min}|_{z=3} &= \begin{cases} \frac{1}{2}, & 0 \leqslant J \leqslant \ln(3)/2 \\ \frac{1}{2}\left[1 - \frac{\mathrm{e}^{2J}[(\mathrm{e}^{2J}+1)(\mathrm{e}^{2J}-3)]^{\frac{1}{2}}}{2[\mathrm{e}^{3J}\sinh(J)-1]}\right], & J \geqslant \ln(3)/2 \end{cases} \\
\varphi_{min}|_{z=4} &= \begin{cases} \frac{1}{2}, & 0 \leqslant J \leqslant \ln(2)/2 \\ \frac{1}{2}\left[1 - \frac{\mathrm{e}^{2J}(\mathrm{e}^{4J}-4)^{\frac{1}{2}}}{\mathrm{e}^{4J}-2}\right], & J \geqslant \ln(2)/2 \end{cases} \\
\varphi_{min}|_{z=6} &= \begin{cases} \frac{1}{2}, & 0 \leqslant J \leqslant \ln(3/2)/2 \\ \frac{\{\mathrm{e}^{2J}+(\mathrm{e}^{4J}+4)^{\frac{1}{2}}-\sqrt{2}[\mathrm{e}^{2J}(\mathrm{e}^{4J}+4)^{\frac{1}{2}}+\mathrm{e}^{4J}-6]^{\frac{1}{2}}\}^6}{4096+\{\mathrm{e}^{2J}+(\mathrm{e}^{4J}+4)^{\frac{1}{2}}+\sqrt{2}[\mathrm{e}^{2J}(\mathrm{e}^{4J}+4)^{\frac{1}{2}}+\mathrm{e}^{4J}-6]^{\frac{1}{2}}\}^6}, & J \geqslant \ln(3/2)/2. \end{cases}
\end{aligned} \tag{D11}$$

Plugging (D11) into Eq. (D9) and noting that $\varphi(0) = 1/2$ we obtain closed-form expressions for the interface steepness at $x = 0$. Similarly, using the definition given by Eq. (D4), we obtain the Cahn-Hilliard interface width for the BG approximation. Results for the interface steepness are shown in Fig. 4(b) with the blue lines and display a strong nonmonotonic trend with respect to J. The broadening of the profile is in sharp contrast to the conclusion drawn by Cahn and Hilliard who write in [1]: *"The interface between two coexisting phases is diffuse and its thickness increases with increasing temperature until at the critical temperature (Tc) the interface is infinite in extent"* (p. 266). Recall that J is expressed in units of $k_B T$, and therefore an increase in temperature corresponds to a decrease in J. To prove that broadening is a general effect regardless of the lattice we take the strong coupling limit of Eq. (D9). For $z > 2$ and $J \to \infty$ the nontrivial solutions to Eq. (D10) are approaching $\chi_\varphi \to 0$ and $\chi_\varphi \to \infty$, resulting in $\varphi_{min} \to 0$ (as with MF). Plugging this into Eq. (D9) together with $\varphi(0) = 1/2$ we obtain

$$\lim_{J\to\infty} \varphi'(0) = \lim_{J\to\infty} \pm\sqrt{2[2zJ - z\,\ln(\mathrm{e}^{2J}+1) + (z-2)\ln(2)]/z_x \sinh(2J)} = 0. \tag{D12}$$

So we find a vanishing interface steepness at $x = 0$ for any lattice with $z > 2$ in the strong coupling limit. For the interface width we find

$$\lim_{J\to\infty} l_{\mathrm{BG,CH}} = \lim_{J\to\infty} (1 - 2\varphi_{\min})/\varphi'(0) = \infty. \tag{D13}$$

Hence, in the strong-interaction limit the interface width diverges for any lattice with $z > 2$.

APPENDIX E: LINEAR STABILITY ANALYSIS

Here we determine the length scales on which inhomogeneities of the concentration profile are stable, as shown in Sec. VI C. We consider a concentration profile of the form $\varphi(\mathbf{x}) = \varphi_0 + a \sin(\mathbf{q}\cdot\mathbf{x})$ with $\mathbf{q} = (q_x, q_y)^{\mathrm{T}}$ and $|a| \ll \min(\varphi_0, 1-\varphi_0)$. A sinusoidal perturbation is taken to agree with the odd boundary conditions which we imposed for Eq. (B12) and (C19). Expanding the local free-energy density and gradient energy coefficient around the homogeneous state up to second order gives

$$\begin{aligned} \mathrm{f}(\varphi(\mathbf{x})) &= \mathrm{f}(\varphi_0) + a \sin(\mathbf{q}\cdot\mathbf{x})\mathrm{f}'(\varphi_0) \\ &\quad + \tfrac{1}{2}a^2 \sin^2(\mathbf{q}\cdot\mathbf{x})\mathrm{f}''(\varphi_0) + O(a^3), \end{aligned} \tag{E1}$$

$$\begin{aligned} &\tfrac{1}{2}\nabla\varphi(\mathbf{x})^{\mathrm{T}}\boldsymbol{\kappa}(\varphi(\mathbf{x}))\nabla\varphi(\mathbf{x}) \\ &\quad = \tfrac{1}{2}a^2[\mathbf{q}^{\mathrm{T}}\boldsymbol{\kappa}(\varphi_0)\mathbf{q}]\cos^2(\mathbf{q}\cdot\mathbf{x}) + O(a^3), \end{aligned} \tag{E2}$$

where $\mathrm{f}'(\varphi_0) \equiv \partial_\varphi \mathrm{f}(\varphi)|_{\varphi_0}$ and $\mathrm{f}''(\varphi_0) \equiv \partial_\varphi^2 \mathrm{f}(\varphi)|_{\varphi_0}$. We want to determine when a sinusoidal perturbation decreases the total free energy compared to the uniform concentration profile. Plugging Eqs. (E1) and (E2) into Eq. (27) and subtracting the free-energy density of the uniform concentration gives

$$\begin{aligned} &F[\varphi(\mathbf{x})] - F[\varphi_0] \\ &= \frac{1}{2L_xL_y}\int_{-\frac{L_y}{2}}^{\frac{L_y}{2}}\int_{-\frac{L_x}{2}}^{\frac{L_x}{2}} \{2a\sin(\mathbf{q}\cdot\mathbf{x})\mathrm{f}'(\varphi_0) \\ &\quad + a^2[\sin^2(\mathbf{q}\cdot\mathbf{x})\mathrm{f}''(\varphi_0) + \cos^2(\mathbf{q}\cdot\mathbf{x})\mathbf{q}^{\mathrm{T}}\boldsymbol{\kappa}(\varphi_0)\mathbf{q}]\}dx\,dy \\ &= \frac{a^2}{4L_xL_y}\{L_xL_y[\mathrm{f}''(\varphi_0) + \mathbf{q}^{\mathrm{T}}\boldsymbol{\kappa}(\varphi_0)\mathbf{q}] \\ &\quad - (q_xq_y)^{-1}\sin(q_xL_x)\sin(q_yL_y)[\mathrm{f}''(\varphi_0) - \mathbf{q}^{\mathrm{T}}\boldsymbol{\kappa}(\varphi_0)\mathbf{q}]\} \\ &= \frac{a^2}{4}[\mathrm{f}''(\varphi_0) + \mathbf{q}^{\mathrm{T}}\boldsymbol{\kappa}(\varphi_0)\mathbf{q}] + O\left(\frac{a^2}{L_xL_y}\right), \end{aligned} \tag{E3}$$

where in the last line we have taken the large system-size limit $(L_x, L_y) \to \infty$. To decrease the total free energy the right-hand side of Eq. (E3) must be negative. Note that $\mathbf{q}^{\mathrm{T}}\boldsymbol{\kappa}(\varphi_0)\mathbf{q} \geqslant 0$, and therefore only $\mathrm{f}''(\varphi_0)$ can make the right-hand side negative. The region where $\mathrm{f}''(\varphi_0) < 0$ in the (φ_0, J) plane is called the spinodal region, and therefore this process is also known as spinodal decomposition. When $\mathrm{f}''(\varphi_0) < 0$ there is an upper bound on stable wave vectors which is given by

$$\mathbf{q}_{\mathrm{crit}}^{\mathrm{T}}\boldsymbol{\kappa}(\varphi_0)\mathbf{q}_{\mathrm{crit}} = -\mathrm{f}''(\varphi_0). \tag{E4}$$

For a one-dimensional perturbation with $q_y = 0$ this translates to $q_{\mathrm{crit}} = \sqrt{-\mathrm{f}''(\varphi_0)/\kappa_x(\varphi_0)}$. The critical wavelength given by $\lambda_{\mathrm{crit}} = 2\pi/q_{\mathrm{crit}}$ provides a lower bound on stable wavelengths. We will now determine the properties of q_{crit} and λ_{crit} for the MF and BG approximations.

1. Results within mean field theory

Taking the MF local free-energy density and square gradient coefficient defined in Eqs. (B9) and (B10) and plugging them into q_{crit} gives the following result:

$$q_{\mathrm{crit,MF}} = \sqrt{-\frac{\mathrm{f}''_{\mathrm{MF}}(\varphi_0)}{\kappa_{\mathrm{MF},x}}} = \sqrt{\frac{4(z_xJ_x + z_yJ_y) - 1/[\varphi_0(1-\varphi_0)]}{z_xJ_x}}. \tag{E5}$$

For isotropic interaction strength $J_x = J_y = J$ and inside the spinodal region $zJ \geqslant 1/[4\varphi_0(1-\varphi_0)]$ the MF critical wave vector is monotonically increasing with J and for $0 < \varphi_0 < 1$ converges to

$$\lim_{J\to\infty} q_{\mathrm{crit,MF}} = 2\sqrt{z/z_x}. \tag{E6}$$

In Fig. 8(b) we plot Eq. (E5) for a square lattice with isotropic interaction strength. The critical wavelength $\lambda_{\mathrm{crit,MF}}$ decreases monotonically with J and converges within the aforementioned range to the value $\lim_{J\to\infty}\lambda_{\mathrm{crit,MF}} = \pi\sqrt{z_x/z}$. In Fig. 4(f) we show the MF critical wavelength for a square lattice with the red line.

2. Results within Bethe-Guggenheim theory

The BG local free-energy density and square gradient coefficient are given by Eqs. (28) and (29). For convenience we immediately take the isotropic interaction strength $J_x = J_y = J$. Plugging the results for the second derivative of the local free-energy density [see Eq. (B17) with $h = 0$ in [77]] into q_{crit} gives Eq. (36). Inside the spinodal region $J \geqslant \ln\{[z-1-\varphi_0(z-2)][1+\varphi_0(z-2)]/[(z-2)^2\varphi_0(1-\varphi_0)]\}/4$ [see Eq. (16) with $h = 0$ in [77]] the BG critical wave vector has a nonmonotonic trend and for $0 < \varphi_0 < 1$ converges to the value

$$\lim_{J\to\infty} q_{\mathrm{crit}} = 0. \tag{E7}$$

In Fig. 8(c) we plot Eq. (36) for a square lattice with isotropic interaction strength. Similarly, the critical wavelength diverges, i.e., $\lim_{J\to\infty}\lambda_{\mathrm{crit}} = \infty$. Hence, for $0 < \varphi_0 < 1$ there exist no finite stable wavelength perturbations in the strong-interaction limit. The coupling strength $J^\dagger(\varphi_0)$ where q_{crit} is maximal, and therefore λ_{crit} minimal, is given by Eq. (37). Remarkably, the maximum of q_{crit}, and therefore the minimum of λ_{crit}, is independent of the uniform concentration value φ_0 and reads as, upon plugging Eq. (37) into Eq. (36),

$$q_{\mathrm{crit}}^{\max} = \frac{2|z-2|}{\sqrt{z_x}}\sqrt{\frac{[z(1+\sqrt{z-1}+z/4)-1]^{\frac{1}{2}} - z/2}{z(2+\sqrt{z-1})-2}}. \tag{E8}$$

The minimum wavelength is easily obtained by $\lambda_{\mathrm{crit}}^{\min} = 2\pi/q_{\mathrm{crit}}^{\max}$. In Fig. 4(f) we depict the BG critical wavelength for a square lattice with the blue line. The coupling value where λ_{crit} attains a minimum is indicated with the blue arrow.

APPENDIX F: ERROR ANALYSIS OF THE APPROXIMATE PARTITION FUNCTIONS IN FINITE SYSTEMS

To probe the accuracy of the MF and BG approximations we compare their partition functions with exact results for the

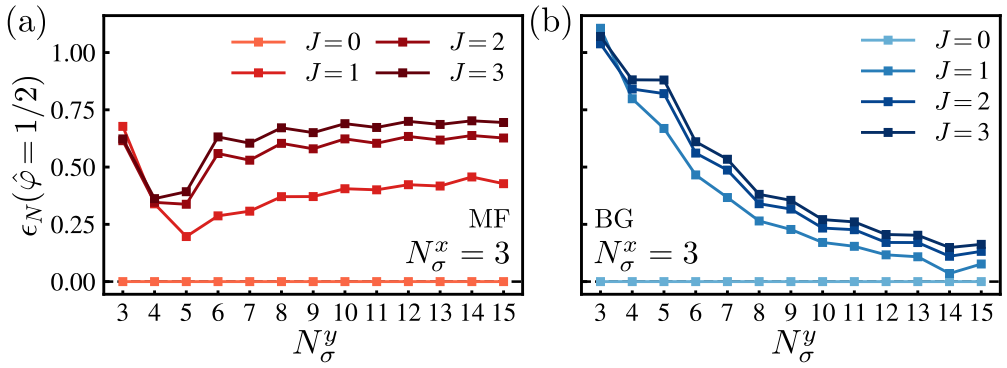

FIG. 9. Relative error between the exact and approximated partition functions obtained with the (a) MF and (b) BG approximations for increasing number of spins and various values of the coupling strength $J = \{0, 1, 2, 3\}$. The relative error in Eq. (F2) is determined for a square lattice composed of $(N_\sigma^x = 3)\times(N_\sigma^y = \{3, \ldots, 15\})$ spins with periodic boundary conditions in the vertical and antisymmetric boundary conditions in the horizontal direction, respectively. The total fraction of down spins is fixed to $\hat{\varphi} = 1/2$.

partition function of finite systems. We limit our error analysis to a one-dimensional concentration profile, conforming with the majority of results discussed in this paper. For a uniform concentration profile an error analysis between the MF and BG approximations is provided in [77] (see Fig. 11 therein). For a lattice composed of $N_\sigma^x \times N_\sigma^y$ spins, let $\boldsymbol{\varphi} = (\varphi_1, \ldots, \varphi_{N_\sigma^x})$ be a vector containing the concentration of downs spins in each column of the lattice. The total concentration of down spins in the lattice is given by $\varphi = ||\boldsymbol{\varphi}||_1/N_\sigma^x$. The exact partition function for a fixed concentration profile along the columns is denoted with $Z(\boldsymbol{\varphi})$ and can be computed via

$$Z(\hat{\boldsymbol{\varphi}}) = \sum_{\boldsymbol{\sigma}} \mathrm{e}^{-\mathcal{H}(\boldsymbol{\sigma})} \prod_{i=1}^{N_\sigma^x} \mathbb{1}_{\hat{\varphi}_i}[\varphi_i], \tag{F1}$$

where we recall that $\boldsymbol{\sigma}$ denotes the matrix containing all spin configurations, $\mathbb{1}_x[z]$ is the indicator function of x, and $\mathcal{H}(\boldsymbol{\sigma})$ is given by Eq. (13). The relative error between $Z_{\mathrm{BG,MF}}(\boldsymbol{\varphi})$ and $Z(\boldsymbol{\varphi})$ for a fixed total concentration of down spins $\hat{\varphi}$ is defined as

$$\epsilon_N(\hat{\varphi}) = \frac{\sum_{\boldsymbol{\sigma}} Z(\boldsymbol{\varphi})\left(1 - \frac{\ln[Z_{\mathrm{MF,BG}}(\boldsymbol{\varphi})]}{\ln[Z(\boldsymbol{\varphi})]}\right)\mathbb{1}_{\hat{\varphi}}[\varphi]}{\sum_{\boldsymbol{\sigma}} Z(\boldsymbol{\varphi})\mathbb{1}_{\hat{\varphi}}[\varphi]}. \tag{F2}$$

Equation (F2) is defined such that differences between $Z(\boldsymbol{\varphi})$ and $Z_{\mathrm{MF,BF}}(\boldsymbol{\varphi})$ attain the largest weight for thermodynamically stable configurations. In Fig. 9 we plot the relative error for the (a) MF and (b) BG approximations for a finite square lattice composed of $(N_\sigma^x = 3)\times(N_\sigma^y = \{3, \ldots, 15\})$ spins with antisymmetric and periodic boundary conditions in the horizontal and vertical direction, respectively. Upon increasing the number of spins in the vertical direction we see that the relative error of the BG approximation decreases towards zero regardless of the coupling strength, whereas the MF approximation saturates to a nonzero value (note that the small system size gives rise to a marked even-odd dependency). For $J = 0$ both approximations are exact and therefore have zero relative error. The improvement of the BG approximation with increasing N_σ^y is due to the fact that it is obtained through a variational principle which is applied in the thermodynamic scaling limit. The MF approximation, on the other hand, becomes worse with increasing N_σ^y due to the approximation for the fraction of defects given by Eq. (B1).

APPENDIX G: NUMERICAL SIMULATIONS OF THE RADIALLY SYMMETRIC CAHN-HILLIARD EQUATION

We study nucleation based on radially symmetric concentration profiles $\varphi(r)$ in two dimensions. Since critical profiles correspond to stationary points of the free energy F given by Eqs. (B11) and (27), we next determine minimal free-energy paths between the homogeneous state and large droplets. We use a measure for the mass concentrated in the nucleus, $N[\varphi] = \int \tanh[w(\varphi - 1/2)]dV$ with $w = 10$, as a reaction coordinate and determine the profile $\varphi(r)$ that minimizes F for a given value N_0 of the constraint using a Lagrange multiplier λ. We thus minimize the constrained free energy

$$F_\lambda[\varphi, \lambda] = F[\varphi] - \lambda(N[\varphi] - N_0) \tag{G1}$$

by evolving the corresponding partial differential equations

$$\partial_t \varphi = \Lambda_D \nabla^2 \frac{\delta F_\lambda}{\delta \varphi}, \tag{G2a}$$

$$\partial_t \lambda = -\Lambda_L \frac{\delta F_\lambda}{\delta \lambda}, \tag{G2b}$$

which corresponds to conserved and nonconserved dynamics with mobilities $\Lambda_D = 10^2$ and $\Lambda_L = 10^4$, respectively. Using this procedure, we determine the profile $\varphi(r)$ with Neumann boundary conditions that optimizes F_λ for each value N_0 of the constraint, which yields the minimal free-energy path. The profile with the largest free energy F corresponds to the saddle point and thus to the critical nucleus that we sought. The corresponding profiles $\varphi(r)$ are shown and analyzed in Fig. 5. Here, the nucleation barrier ΔE is given by the difference of the energy of the critical nucleus to the energy of the homogeneous state.

[1] J. W. Cahn and J. E. Hilliard, Free energy of a nonuniform system. I. interfacial free energy, J. Chem. Phys. **28**, 258 (1958).

[2] J. W. Cahn, Free energy of a nonuniform system. ii. thermodynamic basis, J. Chem. Phys. **30**, 1121 (1959).

[3] J. W. Cahn and J. E. Hilliard, Free energy of a nonuniform system. iii. nucleation in a two-component incompressible fluid, J. Chem. Phys. **31**, 688 (1959).

[4] C. A. Weber, D. Zwicker, F. Jülicher, and C. F. Lee, Physics of active emulsions, Rep. Prog. Phys. **82**, 064601 (2019).

[5] J. S. Rowlinson and B. Widom, *Molecular Theory of Capillarity* (Dover, New York, 2013)

[6] A. J. Bray, Theory of phase-ordering kinetics, Adv. Phys. **51**, 481 (2002).

[7] P. G. de Gennes, Dynamics of fluctuations and spinodal decomposition in polymer blends, J. Chem. Phys. **72**, 4756 (1980).

[8] P. Pincus, Dynamics of fluctuations and spinodal decomposition in polymer blends. II, J. Chem. Phys. **75**, 1996 (1981).

[9] K. Binder, Collective diffusion, nucleation, and spinodal decomposition in polymer mixtures, J. Chem. Phys. **79**, 6387 (1983).

[10] Q. Tang and M. Müller, Evaporation-Induced Liquid Expansion and Bubble Formation in Binary Mixtures, Phys. Rev. Lett. **126**, 028003 (2021).

[11] J. Kirschbaum and D. Zwicker, Controlling biomolecular condensates via chemical reactions, J. R. Soc. Interface **18**, 20210255 (2021).

[12] S. Bo, L. Hubatsch, J. Bauermann, C. A. Weber, and F. Jülicher, Stochastic dynamics of single molecules across phase boundaries, Phys. Rev. Res. **3**, 043150 (2021).

[13] S. Mao, M. S. Chakraverti-Wuerthwein, H. Gaudio, and A. Košmrlj, Designing the Morphology of Separated Phases in Multicomponent Liquid Mixtures, Phys. Rev. Lett. **125**, 218003 (2020).

[14] G. Aubert, P. Kornprobst, and G. Aubert, *Mathematical Problems in Image Processing: Partial Differential Equations and the Calculus of Variations* (Springer, Berlin, 2006), Vol. 147.

[15] M. I. M. Copetti and C. M. Elliott, Numerical analysis of the cahn-hilliard equation with a logarithmic free energy, Numer. Math. **63**, 39 (1992).

[16] H. Gómez, V. M. Calo, Y. Bazilevs, and T. J. Hughes, Isogeometric analysis of the Cahn–Hilliard phase-field model, Comput. Methods Appl. Mech. Eng. **197**, 4333 (2008).

[17] A. W. Adamson and A. P. Gast, *Physical Chemistry of Surfaces* (Wiley, New York, 1967), Vol. 150.

[18] Y. Zhao, P. Stein, and B.-X. Xu, Isogeometric analysis of mechanically coupled Cahn–Hilliard phase segregation in hyperelastic electrodes of li-ion batteries, Comput. Methods Appl. Mech. Eng. **297**, 325 (2015).

[19] Y. Zhao, P. Stein, Y. Bai, M. Al-Siraj, Y. Yang, and B.-X. Xu, A review on modeling of electro-chemo-mechanics in lithium-ion batteries, J. Power Sources **413**, 259 (2019).

[20] A. J. M. Yang, P. D. Fleming, and J. H. Gibbs, Molecular theory of surface tension, J. Chem. Phys. **64**, 3732 (1976).

[21] J. Erlebacher, M. J. Aziz, A. Karma, N. Dimitrov, and K. Sieradzki, Evolution of nanoporosity in dealloying, Nature (London) **410**, 450 (2001).

[22] L.-Q. Chen, Phase-field models for microstructure evolution, Annu. Rev. Mater. Sci. **32**, 113 (2002).

[23] I. Steinbach, Phase-field models in materials science, Model. Simul. Mater. Sci. Eng. **17**, 073001 (2009).

[24] J. D. Murray, *Mathematical Biology I. An Introduction* (Springer, Berlin, 2002).

[25] D. W. Sanders, N. Kedersha, D. S. Lee, A. R. Strom, V. Drake, J. A. Riback, D. Bracha, J. M. Eeftens, A. Iwanicki, A. Wang *et al.*, Competing protein-rna interaction networks control multiphase intracellular organization, Cell **181**, 306 (2020).

[26] W. Hur, J. P. Kemp Jr, M. Tarzia, V. E. Deneke, W. F. Marzluff, R. J. Duronio, and S. Di Talia, Cdk-regulated phase separation seeded by histone genes ensures precise growth and function of histone locus bodies, Dev. Cell **54**, 379 (2020).

[27] W. K. Spoelstra, J. M. Jacques, R. Gonzalez-Linares, F. L. Nobrega, A. C. Haagsma, M. Dogterom, D. H. Meijer, T. Idema, S. J. Brouns, and L. Reese, Crispr-based dna and rna detection with liquid-liquid phase separation, Biophys. J. **120**, 1198 (2021).

[28] D. Stroud, Simple mean-field approach to phase separation in liquid-metal alloys, Phys. Rev. B **8**, 1308 (1973).

[29] J. W. Cahn, Phase separation by spinodal decomposition in isotropic systems, J. Chem. Phys. **42**, 93 (1965).

[30] F. Bergmann, L. Rapp, and W. Zimmermann, Active phase separation: A universal approach, Phys. Rev. E **98**, 020603(R) (2018).

[31] J. Stenhammar, A. Tiribocchi, R. J. Allen, D. Marenduzzo, and M. E. Cates, Continuum Theory of Phase Separation Kinetics for Active Brownian Particles, Phys. Rev. Lett. **111**, 145702 (2013).

[32] S. A. Safran, *Statistical Thermodynamics of Surfaces, Interfaces, and Membranes* (CRC Press, Boca Raton, FL, 2018).

[33] W. L. Bragg and E. J. Williams, The effect of thermal agitation on atomic arrangement in alloys, Proc. Math. Phys. Eng. Sci. **145**, 699 (1934).

[34] P. J. Flory, *Principles of Polymer Chemistry* (Cornell University Press, Ithaca, NY, 1953).

[35] P. J. Flory, Thermodynamics of high polymer solutions, J. Chem. Phys. **10**, 51 (1942).

[36] W. M. Jacobs, Self-Assembly of Biomolecular Condensates with Shared Components, Phys. Rev. Lett. **126**, 258101 (2021).

[37] X. Wei, J. Zhou, Y. Wang, and F. Meng, Modeling Elastically Mediated Liquid-Liquid Phase Separation, Phys. Rev. Lett. **125**, 268001 (2020).

[38] K. Tripathi and G. I. Menon, Chromatin Compaction, Auxeticity, and the Epigenetic Landscape of Stem Cells, Phys. Rev. X **9**, 041020 (2019).

[39] Y. Zhang, B. Xu, B. G. Weiner, Y. Meir, and N. S. Wingreen, Decoding the physical principles of two-component biomolecular phase separation, eLife **10**, e62403 (2021).

[40] J. Meibohm and M. Esposito, Finite-Time Dynamical Phase Transition in Nonequilibrium Relaxation, Phys. Rev. Lett. **128**, 110603 (2022).

[41] A. Parry and C. Rascón, The Goldstone mode and resonances in the fluid interfacial region, Nat. Phys. **15**, 287 (2019).

[42] G. Münster and M. Cañizares Guerrero, Interface roughening in two dimensions, J. Stat. Phys. **182**, 1 (2021).

[43] P. Ronceray, Y. Zhang, X. Liu, and N. S. Wingreen, Stoichiometry Controls the Dynamics of Liquid Condensates of Associative Proteins, Phys. Rev. Lett. **128**, 038102 (2022).

[44] N. Lauber, O. Tichacek, R. Bose, C. Flamm, L. Leuzzi, K. Ruiz-Mirazo, D. De Martino *et al.*, Statistical mechanics of biomolecular condensates via cavity methods, arXiv:2201.11581.

[45] Y.-H. Lin, J. D. Forman-Kay, and H. S. Chan, Theories for sequence-dependent phase behaviors of biomolecular condensates, Biochemistry **57**, 2499 (2018).

[46] Y.-H. Lin, J. D. Forman-Kay, and H. S. Chan, Sequence-Specific Polyampholyte Phase Separation in Membraneless Organelles, Phys. Rev. Lett. **117**, 178101 (2016).

[47] M. Müller and L. G. MacDowell, Interface and surface properties of short polymers in solution: Monte Carlo simulations and self-consistent field theory, Macromolecules **33**, 3902 (2000).

[48] A. Squarcini and A. Tinti, Correlations and structure of interfaces in the Ising model: Theory and numerics, J. Stat. Mech. (2021) 083209.

[49] E. A. Guggenheim, The statistical mechanics of regular solutions, Proc. Math. Phys. Eng. Sci. **148**, 304 (1935).

[50] H. A. Bethe, Statistical theory of superlattices, Proc. Math. Phys. Eng. Sci. **150**, 552 (1935).

[51] R. Kikuchi and J. W. Cahn, Theory of domain walls in ordered structures–II: Pair approximation for nonzero temperatures, J. Phys. Chem. Solids **23**, 137 (1962).

[52] J. Parlange, Phase transition and surface tension in the quasi-chemical approximation, J. Chem. Phys. **48**, 169 (1968).

[53] D. Zwicker, py-pde: A python package for solving partial differential equations, J. Open Source Software **5**, 2158 (2020).

[54] K. Binder, R. Evans, D. P. Landau, and A. M. Ferrenberg, Interface localization transition in ising films with competing walls: Ginzburg criterion and crossover scaling, Phys. Rev. E **53**, 5023 (1996).

[55] E. Albano, K. Binder, D. Heermann, and W. Paul, Critical wetting in the square Ising model with a boundary field, J. Stat. Phys. **61**, 161 (1990).

[56] J. Rogiers and J. Indekeu, Effect of gravity and confinement on phase equilibria, Europhys. Lett. **24**, 21 (1993).

[57] G. Bilalbegović, Interface delocalization in the three-dimensional Ising model, J. Stat. Phys. **50**, 1131 (1988).

[58] K. Binder, D. P. Landau, and A. M. Ferrenberg, Character of the Phase Transition in Thin Ising Films with Competing Walls, Phys. Rev. Lett. **74**, 298 (1995).

[59] K. Binder, M. Müller, F. Schmid, and A. Werner, Interfacial profiles between coexisting phases in thin films: Cahn-Hilliard treatment versus capillary waves, J. Stat. Phys. **95**, 1045 (1999).

[60] A. Ciach, Correlation functions in the solid-on-solid model of the fluctuating interface, Phys. Rev. B **34**, 1932 (1986).

[61] J. Stecki, Capillary length of a planar interface from low temperatures to the critical point: An Ising d=2 strip, Phys. Rev. B **47**, 7519 (1993).

[62] J. Stecki, A. Maciolek, and K. Olaussen, Magnetization profiles of the planar fluctuating interface in a d=2 Ising strip, Phys. Rev. B **49**, 1092 (1994).

[63] A. Ciach and J. Stecki, Scaling in the solid-on-solid interfaces, J. Phys. A: Math. Theor. **20**, 5619 (1987).

[64] E. Albano, K. Binder, and W. Paul, Monte Carlo studies of d= 2 Ising strips with long-range boundary fields, J. Phys.: Condens. Matter **12**, 2701 (2000).

[65] M. E. Fisher, Walks, walls, wetting, and melting, J. Stat. Phys. **34**, 667 (1984).

[66] M. E. Fisher, Interface wandering in adsorbed and bulk phases, pure and impure, J. Chem. Soc. Faraday Trans. II **82**, 1569 (1986).

[67] F. Schmitz, P. Virnau, and K. Binder, Logarithmic finite-size effects on interfacial free energies: Phenomenological theory and Monte Carlo studies, Phys. Rev. E **90**, 012128 (2014).

[68] R. Lipowsky, D. M. Kroll, and R. K. P. Zia, Effective field theory for interface delocalization transitions, Phys. Rev. B **27**, 4499 (1983).

[69] D. B. Abraham, Capillary Waves and Surface Tension: An Exactly Solvable Model, Phys. Rev. Lett. **47**, 545 (1981).

[70] M. P. A. Fisher, D. S. Fisher, and J. D. Weeks, Agreement of Capillary-Wave Theory with Exact Results for the Interface Profile of the Two-Dimensional Ising Model, Phys. Rev. Lett. **48**, 368 (1982).

[71] X. Wang, Asymptotics of the q-theta function, Commun. Math. Anal. **7**, 50 (2009).

[72] A. Mukhopadhyay and B. M. Law, Casimir effect in critical films of binary liquid mixtures, Phys. Rev. E **62**, 5201 (2000).

[73] D. M. Dantchev and S. Dietrich, Critical casimir effect: Exact results, Phys. Rep. **1005**, 1 (2023).

[74] L. P. Kadanoff, Scaling laws for ising models near T_c, Phys. Phys. Fiz. **2**, 263 (1966).

[75] R. Kikuchi, A theory of cooperative phenomena, Phys. Rev. **81**, 988 (1951).

[76] E. Artin, *The Gamma Function* (Dover, New York, 2015).

[77] K. Blom and A. Godec, Criticality in Cell Adhesion, Phys. Rev. X **11**, 031067 (2021).

[78] H. Kramers, Brownian motion in a field of force and the diffusion model of chemical reactions, Physica (Amsterdam) **7**, 284 (1940).

[79] J. Langer, Statistical theory of the decay of metastable states, Ann. Phys. **54**, 258 (1969).

[80] P. Hänggi, P. Talkner, and M. Borkovec, Reaction-rate theory: Fifty years after Kramers, Rev. Mod. Phys. **62**, 251 (1990).

[81] D. Hartich and A. Godec, Duality between relaxation and first passage in reversible markov dynamics: Rugged energy landscapes disentangled, New J. Phys. **20**, 112002 (2018).

[82] C. N. Yang, The spontaneous magnetization of a two-dimensional Ising model, Phys. Rev. **85**, 808 (1952).

[83] V. Spirin, P. L. Krapivsky, and S. Redner, Fate of zero-temperature Ising ferromagnets, Phys. Rev. E **63**, 036118 (2001).

[84] K. Barros, P. L. Krapivsky, and S. Redner, Freezing into stripe states in two-dimensional ferromagnets and crossing probabilities in critical percolation, Phys. Rev. E **80**, 040101(R) (2009).

[85] N. Metropolis, A. W. Rosenbluth, M. N. Rosenbluth, A. H. Teller, and E. Teller, Equation of state calculations by fast computing machines, J. Chem. Phys. **21**, 1087 (1953).

[86] M. Müller and G. Münster, Profile and width of rough interfaces, J. Stat. Phys. **118**, 669 (2005).